New experimental data and semi-empirical parameterization of H_2O–CO_2 solubility in mafic melts

Giada Iacono-Marziano [a,*], Yann Morizet [b], Emmanuel Le Trong [a],
Fabrice Gaillard [a]

[a] *ISTO, UMR 7327 CNRS-Université d'Orléans, 1a rue de la Ferollerie, Orléans, France*
[b] *Université de Nantes, Nantes Atlantique Universités, Laboratoire de Planétologie et Géodynamique de Nantes (LPGN), UMR CNRS 6112, 2 rue de la Houssinière, 44322 Nantes, France*

Abstract

We present here new experimental data on H_2O–CO_2 solubility in mafic melts with variable chemical compositions (alkali basalt, lamproite and kamafugite) that extend the existing database. We show that potassium and calcium-rich melts can dissolve ~1 wt% CO_2 at 3500 bar (350 MPa) and 1200 °C, whereas conventional models predict solubilities of 0.2–0.5 wt%, under similar P–T conditions. These new data, together with those in the literature, stress the fundamental control of melt chemical composition on CO_2 solubility. We present a semi-empirical H_2O–CO_2 solubility model for mafic melts, which employs simplified concepts of gas–melt thermodynamics coupled with a parameterization of both chemical composition and structure of the silicate melt. The model is calibrated on a selected database consisting of 289 experiments with 44 different mafic compositions. Statistical analyses of the experimental data indicate that, in mafic melts, the chemical composition and therefore the structure of the melt plays a fundamental role in CO_2 solubility. CO_2 solubility strongly depends on the amount of non-bridging oxygen per oxygen (NBO/O) in the melt, but the nature of the cation bonded to NBO is also critical. Alkalis (Na + K) bonded to NBO result in a strong enhancement of CO_2 solubility, whereas Ca has a more moderate effect. Mg and Fe bonded to NBO have the weakest effect on CO_2 solubility. Finally, we modelled the effect of water and concluded that H_2O dissolution in the melt enhances CO_2 solubility most likely by triggering NBO formation. In contrast with CO_2 but in agreement with earlier findings, H_2O solubility in mafic melts is negligibly affected by melt composition and structure: it only shows a weak correlation with NBO/O.
© 2012 Elsevier Ltd. All rights reserved.

1. INTRODUCTION

The dynamics of volcanic systems strongly depend on magmatic volatiles because of the ability of the latter to segregate as a low density fluid phase if their amounts exceed the relevant solubility limits in the silicate melt (Phillips and Woods, 2002; Menand and Phillips, 2007). Solubility laws of volatiles generally describe increasing amounts of dissolved components in volatile saturated melts as pressure and, therefore, depth increases (Behrens and Gaillard, 2006). Accurate volatile solubility laws are inescapably needed to robustly model volatile degassing upon magma ascent (Moretti and Papale, 2004; Burgisser et al., 2008; Gaillard and Scaillet, 2009) and to interpret volatile contents of melt inclusions and constrain their entrapment depths (Moore, 2008; Métrich and Wallace, 2008). The most abundant volatile component in magmatic systems is H_2O generally followed by CO_2 (Métrich and Wallace, 2008), although, some volcanic systems can intermittently degas more CO_2 than H_2O (Edmonds and Gerlach, 2007; Liotta et al., 2010). On the basis of general solubility trends, elevated CO_2/H_2O ratios in volcanic plumes are generally interpreted to indicate deep degassing (Aiuppa et al.,

2006; Edmonds and Gerlach, 2007; Shinohara et al., 2008). However, other mechanisms can be conducive to high CO_2 contents in volcanic gases: open system degassing (Edmonds and Gerlach, 2007), large gas content in magma chambers at depth prior to eruption (Wallace, 2003; Scaillet and Pichavant, 2003), or interactions with sedimentary carbonates (Iacono-Marziano et al., 2009). Accurate solubility laws are essential to decipher which of the above mentioned processes controls volcanic degassing. Due to the strong influence of melt composition on CO_2 solubility (Dixon, 1997; Brooker et al., 2001a,b and new data in this study), the high-temperature high-pressure experimental approach is critical but solubility models are nevertheless needed to extrapolate or interpolate experimental data and predict H_2O and CO_2 solubility for variable chemical compositions under different conditions.

We present here new experimental data on specific melt compositions that clarify the chemical control on CO_2 solubility and show the limitation of existing models in predicting such chemical effects. We focus on mafic systems ranging from andesitic to picritic compositions and we propose an empirical model for H_2O–CO_2 solubility built on thermodynamics and considerations of melt structure calibrated on a comprehensive database. Our approach is to develop a pragmatic model for H_2O–CO_2 solubility in mafic melts, which avoids excessively complex thermodynamic formulations, but can nevertheless reproduce experimental data. We show that the use of structural parameters in addition to chemical components may be used to retrieve the existing database with a relatively simple and flexible thermodynamic framework.

1.1. Existing models for H_2O–CO_2 solubility in silicate melts

H_2O solubility models in silicate melts have been pioneered by Burnham and Davis (1971) who propose that, at low water contents, water solubility in silicate melts depends on the square root of water pressure or fugacity. By carrying out a systematic infrared absorption study of water dissolved in silicate melts, Stolper (1982) proposed a thermodynamic model for water dissolution involving both molecular H_2O and OH species, which applies at higher water contents. Empirical and simpler formulations have been more recently developed (Moore et al., 1998) and reveal a minor control of melt chemical compositions on water solubility.

Most CO_2 and H_2O–CO_2 solubility models are calibrated on databases that do not integrate the recent and high quality literature published since 2006. Dixon (1997) proposes a semi-empirical chemical model for CO_2 solubility at 1 kbar based on thermodynamic formulations previously described by Spera and Bergman (1980). The introduction of the empirical factor Π accounts for the enhancement of CO_2 solubility in melts as Ca, K, Na, Mg and Fe (listed in the order of the magnitude of their effect) are added to the system. The Π parameter also predicts that increasing Si and Al melt contents would decrease CO_2 solubility. The main limitation of this model is that it is restricted to low pressure conditions (<1000 bar) corresponding to low dissolved H_2O and CO_2 contents. Lesne et al.

(2011a) propose a re-adjustment of the Π factor of Dixon (1997) in order to reproduce more recent experimental data and suggested that it could be reasonably extrapolated to 2000 bar, however no rigorous tests of its validity have been done so far over a comprehensive database.

VolatileCalc (Newman and Lowenstern, 2002) is probably the most used H_2O–CO_2 solubility model and has the great advantages of being easy to use and founded on thermodynamic basis, previously developed by Stolper (1982) for water. The main drawback of VolatileCalc is that it poorly takes into account how changes in melt composition affect H_2O and CO_2 solubility, the SiO_2 content of the melt being the only chemical parameter considered. In this paper, we present experimental data showing that melt SiO_2 content is not sufficient to accurately predict CO_2 solubility.

Papale et al. (2006) published the most sophisticated solubility model for H_2O–CO_2 gas mixture in multi-component molten silicate, accounting for the chemical control operated by eight melt components (oxides, e.g. SiO_2, Al_2O_3) on H_2O and CO_2 solubility. The model has initially been developed for one-component solubility, i.e. H_2O–silicate melt and CO_2–silicate melt (Papale, 1997), and it has evolved to a two component model, i.e. H_2O–CO_2 mixture – silicate melt (Papale, 1999; Papale et al. (2006)). In all cases, the effect of a given melt component on H_2O and CO_2 solubilities is calibrated by fitting experimental data within a thermodynamic framework. In Papale et al. (2006) 26 regression parameters account for the dependence of both H_2O and CO_2 solubilities on melt composition and additional fitted parameters for standard thermodynamic properties (enthalpy, entropy, heat capacity, volume terms). The mixing formalism used in Papale et al. (2006) is a regular symmetric one (as in Ghiorso and Sack, 1995): the interaction parameters (Margules parameters) are adjusted between each pair of components assuming that a binary mixture would show similar interactions if diluted in multi-component systems. In all, these three models (Dixon, 1997; Newman and Lowenstern, 2002; Papale et al., 2006) are essentially chemical models, which account, with variable degree of complexity, for the effects of melt composition on H_2O–CO_2 solubility.

1.2. Melt structure and CO_2 solubility

A different approach has been also deployed to evaluate the control of melt structure and chemical composition on CO_2 solubility. Structural studies (Brooker et al., 1999, 2001a) and recent molecular dynamic simulations (Guillot and Sator, 2011) clearly reveal the melt structural controls on CO_2 solubility in mafic melts.

In mafic compositions, CO_2 is observed to dissolve in the melt uniquely as CO_3^{2-}. The amount of available oxygens and the type of cation bonded to these oxygens are therefore key factors in controlling CO_2 solubility (Brooker et al., 2001a,b). In this paragraph, we present a synthetic overview of the current knowledge of silicate melt structure that has to be taken into account for modelling the effect of the chemical composition on CO_2 solubility. Spectroscopic methods (FTIR, Raman, NMR and X-ray analyses) describe the silicate melt as a complex assembly of individual

tetrahedral unit called Q^n species (e.g. Farnan and Stebbins, 1994; Frantz and Mysen, 1995; Mysen, 2003), with n standing for the number of bridging oxygen (BO) between 0 and 4 within the tetrahedron, the number of non-bridging oxygens being therefore NBO = 4 − BO. The chemical composition of the melt controls the abundances of the different Q^n species and therefore both the abundance and the nature of the NBO. Lee and Sung (2008) show that several types of NBOs are present within the melt structure depending on the surrounding cation. Increasing the concentration of the alkalis or alkaline-earth elements increases the number of depolymerised Q^n units within the melt (e.g. Grimmer et al., 1984; Maekawa et al., 1991; Schneider et al., 2003; Halter and Mysen, 2004; Neuville et al., 2006; Malfait et al., 2007). Alkalis and alkaline-earths can be either charge balancing cations or network modifying cations (Maekawa et al., 1997; Lee and Sung, 2008; Lee and Stebbins, 2009). The change in the coordination number of the alkalis and alkaline-earth elements within the melt is regarded as an effect of the cation field strength (Shimoda et al., 2008). Si and Al are generally considered as network formers (Rossano et al., 1999; Guillot and Sator, 2007), although very high pressures favour V and VI coordinated network forming cations (McMillan and Wilding, 2009). The presence of highly coordinated Al (V and VI) is also correlated to the concentration of charge balancing cations. Recent work (Toplis et al., 2000; Neuville et al., 2010) suggests that V coordinated Al concentration increases in Ca–MgO–Al_2O_3–SiO_2 and Ca–Al_2O_3 glasses with decreasing Mg or Ca content. The major implication of this result is that Al adopts a network modifying rather than a network forming character. However, the concentration of V coordinated Al remains relatively low (<9% of the total Al) in such glasses. In peraluminous melts, the possible presence of 3-coordinated oxygen atoms has also been invoked by Toplis et al. (1997) forming Al, Si triclusters. This assumption based on viscosity measurements is corroborated by the fact that low alkali concentrations are not sufficient to balance the charge deficiency in AlO_4 tetrahedra.

The structural behaviour of Mg in silicate melt is currently less constrained than Ca or Na. Stebbins and co-workers (Fiske and Stebbins, 1994; Georges and Stebbins, 1998; Kroeker and Stebbins, 2000; McMillan and Wilding, 2009) suggested that Mg exhibited several coordination numbers (changing mainly between five and six) as a function of the chemical composition. Mg atoms, like Ca and Na, also give rise to several NBO within the melt (Kelsey et al., 2008) and are seen to influence the coordination sphere of network forming atoms such as Al (Guignard and Cormier, 2008).

The configuration of carbonate units has been extensively discussed in previous works (Kohn et al., 1991; Brooker et al., 1999, 2001b). Fourier transform infrared (FTIR) studies show that CO_2 dissolves in mafic melts as carbonate groups with two configurations: (1) network carbonates, i.e. T–CO_3–T (where T is a tetrahedron, principally Si^{4+}, Al^{3+}), (2) carbonate groups connected to a non-bridging oxygen, i.e. NBO–CO_3 M^{n+} (where M^{n+} is a charge balancing or network modifying cation such as Na^+, K^+ or Ca^{2+}). Brooker et al. (2001a) propose that

CO_2 solubility is a function of the degree of polymerisation of the melt, on the basis of a strong increase in CO_2 solubility with increasing NBO/T. In basaltic and more mafic compositions, such as those studied here, the NBO–CO_3 association constitutes the principal mechanism of CO_2 dissolution in the glass (Morizet et al., 2010). This spectroscopic observation is entirely consistent with theoretical simulations conducted using molecular dynamics simulations (Guillot and Sator, 2011).

2. NEW DATA ON H_2O–CO_2 SOLUBILITY

2.1. Experimental and analytical methods

Fluid saturated experiments in the system H_2O–CO_2 were conducted in internally heated pressure vessels (ISTO, Orléans), at 1200 °C and 485–4185 bar. Au_{80}–Pd_{20} capsules (internal diameter 2.5 mm), were used in order to minimise iron loss from the melt to the capsule during the run. All experiments were ended by drop quench. By using pure argon as a pressure medium without hydrogen addition, oxidised conditions were achieved, i.e. $fO_2 > FMQ + 1$ (Gaillard et al., 2003); no effort was made to control oxygen fugacity. Two starting glasses, an alkali-basalt from Mt. Etna, Italy (see Lesne et al., 2011a) and a lamproite from Torre Alfina, Italy, (see Peccerillo et al., 1998) were used (compositions in Table 1), corresponding to two different types of experiments. In the first case, 100–150 mg of alkali-basaltic starting glass were loaded together with variable amounts of water and/or dehydrated oxalic acid, or silver carbonate and the experiments were performed at 1200 °C and variable pressures (between 485 and 4185 bar) (Table 2). Experiments lasted 18–76 h; the difference in the experimental duration does not significantly affect iron loss from the melt (the compositions of the experimental samples are within the standard deviation of the Etna starting glass composition in Table 1). The aim of these experiments was to characterise H_2O–CO_2 solubility in alkali-basaltic melts as a function of pressure at typical magmatic conditions. Recovered glasses were checked by both optical

Table 1
Composition of the starting glasses.

Sample	Etna[c]	Torre Alfina
SiO_2[a]	47.95 (82)	55.65 (47)
TiO_2[a]	1.67 (11)	1.34 (9)
Al_2O_3[a]	17.32 (27)	13.03 (25)
FeO^*[a]	10.24 (125)	5.82 (36)
MgO[a]	5.76 (28)	9.41 (29)
CaO[a]	10.93 (37)	5.44 (36)
Na_2O[a]	3.45 (16)	0.96 (10)
K_2O[a]	1.99 (10)	7.67 (23)
P_2O_5[a]	0.51 (12)	0.51 (7)
TOTAL[a]	99.82 (93)	97.15 (88)
H_2O wt%[b]	0.010 (1)	3.21 (23)
CO_2 ppm	bdl	bdl

bdl: below detection limit.
[a] Analysed by EMP.
[b] Analysed by FTIR spectroscopy.
[c] From Lesne et al. (2011b).
* Total

Table 2
Experimental conditions and results of experiments with Mt. Etna basalt.

P_{total} (bar)	485	485	485	485	1015	1015	1015	1017	1017	1530	1530	1530	1530
Duration (h)	70	70	70	70	50	50	50	26	26	56	56	56	56
H$_2$O added wt%	–	2.32	3.77	3.63	–	2.99	4.85	–	2.87	–	3.22	5.44	5.50
CO$_2$ added wt%	1.82	2.45	–	–	1.04	3.59	–	2.1	2.92	1.75	2.93	–	–
CO$_2$ source	Ag$_2$CO$_3$	DOA	–	–	Ag$_2$CO$_3$	DOA	–	Ag$_2$CO$_3$	DOA	Ag$_2$CO$_3$	DOA	–	–
X_{CO2} gas	0.68	0.56	–	–	0.84	0.49	–	0.88	0.51	0.81	0.43	–	–
P_{CO2}	330	271	–	–	851	501	–	898	516	1244	658	–	–
St. dev. P_{CO2}	50	41	–	–	128	75	–	135	77	187	99	–	–
wt% H$_2$O glass	0.95	1.18	2.22	2.02	0.99	2.12	3.48	0.80	2.08	1.43	3.01	4.46	4.87
St. dev. H$_2$O	0.05	0.07	0.09	0.11	0.06	0.17	0.22	0.05	0.08	0.07	0.26	0.37	0.35
ppm CO$_2$ glass	306	191	–	–	843	548	–	808	534	1278	1035	–	–
St. dev. CO$_2$	43	27	–	–	118	82	–	121	75	179	145	–	–
P_{tot} (bar)	2047	2047	2055	2055	2135	2135	2754	3080	3080	4185	4185	4185	4185
Duration (h)	44	44	22	22	66	66	71	76	76	18	18	18	18
H$_2$O added wt%	–	3.73	–	3.59	4.25	7.21	–	–	3.86	–	–	3.82	2.43
CO$_2$ added wt%	1.00	3.89	1.03	3.74	3.86	–	3.08	1.86	2.08	0.67	0.92	6.22	1.74
CO$_2$ source	Ag$_2$CO$_3$	DOA	Ag$_2$CO$_3$	DOA	DOA	–	Ag$_2$CO$_3$	Ag$_2$CO$_3$	DOA	Ag$_2$CO$_3$	Ag$_2$C$_2$O$_3$	DOA	DOA
X_{CO2} gas	0.90	0.61	0.93	0.48	0.65	–	0.87	0.94	0.64	0.94	0.93	0.76	0.87
P_{CO2}	1843	1258	1920	984	1393	–	2403	2903	1970	3919	3888	3182	3656
St. dev. P_{CO2}	276	189	288	148	209	–	360	435	296	588	583	477	548
wt% H$_2$O glass	1.04	2.82	0.87	3.45	2.70	5.09	1.64	1.09	3.54	1.36	1.47	3.31	2.16
St. dev. H$_2$O	0.14	0.09	0.08	0.07	0.19	0.42	0.08	0.09	0.30	0.07	0.10	0.21	0.18
ppm CO$_2$ glass	1853	1489	1706	1408	1412	–	2515	2816	2416	3673	3965	4061	4230
St. dev. CO$_2$	259	208	239	197	198	–	352	394	338	615	663	686	711

DOA: dehydrated oxalic acid.
All experiments were performed at 1200 °C.

and scanning electron microscopy to be crystal- and bubble-free.

In the second type of experiments, 60–100 mg of pre-hydrated (3.2 wt% water) lamproitic glass were loaded with variable amounts of dolomite and calcite (Table 3) and equilibrated at 1200 °C and 3150 bar. Dolomite and calcite introduce calcium and magnesium to the system, in addition to CO_2, and therefore modifies the composition of the melt (Table 3). Experiments lasted 3 h, sufficient to ensure complete carbonate dissolution in the melt (confirmed by the homogeneous Ca, Mg and CO_2 contents of the melts in Table 3). Sample #2TA3 contains 5% of olivine crystals whereas the other samples are crystal free. The aim of these experiments was to reveal the strong effect of melt composition on CO_2 solubility.

Major element compositions of the glasses was analysed with a Cameca SX-50 electron microprobe (EMP), using the following operating conditions: 15 kV accelerating voltage, 7 nA beam current, 10 s counting time for all elements on each spot, and 10 μm spot size. Sodium was analysed first to limit any loss.

Table 3
Experimental conditions and results of the experiments with Torre Alfina lamproite.

Sample	2TA1	2TA2	2TA3
P total (bar)	3510	3510	3510
P CO_2 (bar)	2633	3299	3370
P H_2O (bar)	878	211	140
Temperature (°C)	1200	1200	1200
Duration (h)	3	3	3
Calcite added wt%	2.47	4.91	10.43
Dolomite added wt%	4.17	8.01	15.65
CO_2 added wt%	3.08	5.98	12.05
Glass composition[a]	6 analyses	6 analyses	6 analyses
SiO_2	54.48 (43)	51.71 (32)	47.36 (66)
TiO_2	1.38 (9)	1.22 (9)	1.22 (13)
Al_2O_3	13.00 (30)	12.38 (26)	11.55 (29)
FeO	5.31 (13)	5.38 (22)	5.04 (14)
MgO	8.43 (25)	9.27 (35)	10.90 (35)
CaO	8.07 (51)	11.41 (29)	15.92 (62)
Na_2O	0.86 (11)	0.82 (7)	0.83 (9)
K_2O	7.87 (11)	7.21 (12)	6.58 (26)
P_2O_5	0.60 (6)	0.60 (6)	0.60 (8)
Total	96.02 (94)	97.06 (87)	97.65 (93)
H_2O wt%[b]	2.83 (15)	2.52 (13)	2.49 (10)
CO_2 wt% [b] (Fine and Stolper, 1986)[c]	0.30 (1)	0.49 (1)	0.90 (3)
CO_2 wt% [b] (Thibault and Holloway, 1994)[d]	0.31 (1)	0.52 (2)	0.95 (3)
CO_2 wt% [b] (Behrens et al., 2009)[e]	0.34 (1)	0.59 (1)	1.08 (4)

[a] Analysed by EMP.
[b] Analysed by FTIR spectroscopy.
[c] Using ε_{1430} in Fine and Stolper (1986) for basaltic melts.
[d] Using ε_{1515} in Thibault and Holloway (1994) for Ca-rich leucititic melts.
[e] Using ε_{1430} in Behrens et al. (2009) for phonotephritic melts.

H_2O and CO_2 concentrations in the quenched glasses were determined by transmission FTIR spectroscopy on doubly polished glass chips, using a Nicolet 760 Magna spectrometer equipped with an IR microscope and a MCT detector. Absorption spectra were acquired for each sample in the range 1000–6000 cm^{-1} with 128 scans and a resolution of 4 cm^{-1}. A Globar light source and a KBr beamsplitter was used for the mid-infrared (MIR), while a tungsten white light source and a CaF_2 beam-splitter for the near-infrared (NIR). For each sample 6–15 spots were analysed to verify the homogeneity of the H_2O and CO_2 contents in the glass (standard deviations in Tables 2 and 3). In samples with water contents higher than 1.2 wt%, total water was determined as the sum of structurally bonded hydroxyl groups and molecular water concentrations, and therefore calculated using the Lambert–Beer law from the absorbances of the 4470 and 5210 cm^{-1} bands, respectively. In water-poor samples (<1.2 wt%), total water was calculated from the absorbance of the fundamental OH-stretching vibration at about 3530 cm^{-1}. For the three peaks (4470, 5210 and 3530 cm^{-1}), the heights were determined using linear background corrections (as in Lesne et al., 2011a). We used the linear extinction coefficient in Fine and Stolper (1986), for the 3530 cm^{-1} band and those in Lesne et al. (2011a) for the 4470 and 5210 cm^{-1} bands, which were calibrated for our alkali-basaltic composition.

CO_2 is dissolved in mafic melts as carbonate groups (CO_3^{2-}), which have two asymmetric stretching vibrations with different frequency that give the characteristic "carbonate doublet" (Blank and Brooker, 1994 and references therein). The difference in frequency ($\Delta\nu_3$) is proportional to the distortion of the carbonate structure (i.e. the difference in environment among the carbonate oxygens, Brooker et al., 1999, 2001a,b; Morizet et al., 2010). For our compositions, the peaks of the carbonate doublet are at about 1515 and 1430 cm^{-1}. The major source of error in CO_2 calculation is represented by the background correction to constrain peak heights of the CO_3^{2-} doublet. For high CO_2 contents, the carbonate peaks overlap, while for high water contents, the water peak at 1630 cm^{-1} (due to the ν_2 bending of H_2O molecules, Ihinger et al., 1994) interferes with the higher wave number carbonate peak (Fig. 1). Possible background corrections consist in the deconvolution of the three peaks (e.g. Jakobsson, 1997; Morizet et al., 2010), the use of French lines (e.g. King and Holloway, 2002), or the subtraction of a volatile-free spectrum, which is the most employed technique (e.g. Fine and Stolper, 1986; Thibault and Holloway, 1994; Dixon and Pan, 1995; Jendrzejewski et al., 1997; Behrens et al., 2009). However, for H_2O-bearing samples the inaccuracy in the estimation of the 1515 cm^{-1} peak height is higher if the height of the peak at 1630 cm^{-1} is different between the sample and the subtracted spectrum (Fig. 1). Extinction coefficients for the carbonate doublet were determined by several authors for various mafic compositions, i.e. basalt, Ca-rich leucitite, basanite, icelandite, andesite, phonotephrite, shoshonite, generally in almost anhydrous samples (Fine and Stolper, 1986; Thibault and Holloway, 1994; Dixon and Pan, 1995; Jendrzejewski et al., 1997; Jakobsson, 1997; King and Holloway, 2002; Behrens et al., 2009;
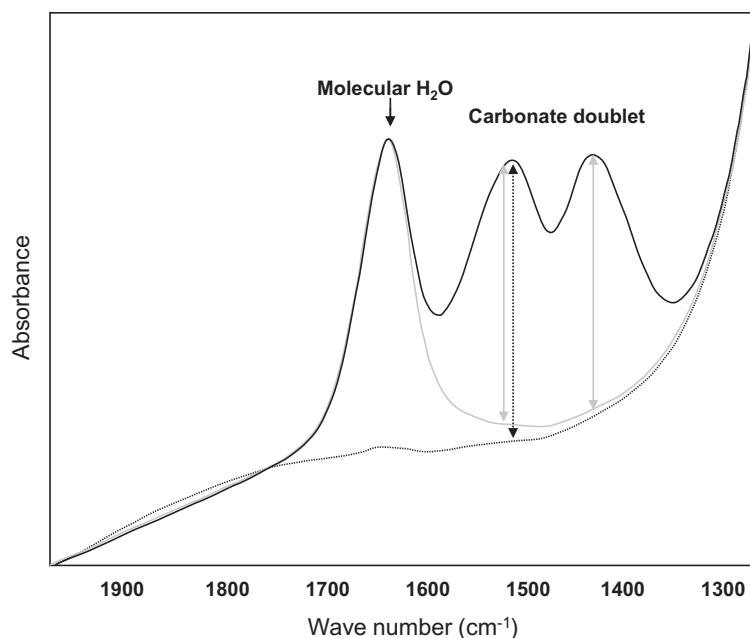
Fig. 1. Representative infrared absorption spectra (scaled to the same thickness) of alkali-basaltic glasses (Mt. Etna composition) in the 1900–1300 cm^{-1} region. Black line shows a H_2O–CO_2-rich glass; grey line a H_2O-rich, CO_2-free glass; pointed line a H_2O–CO_2-free glass (starting glass). The positions of the H_2O and carbonate bands are shown. In this study, we calculated peak heights for the carbonate doublet, by manually subtracting the spectrum of a CO_2-free glass containing a similar amount of water to the sample spectrum (e.g. black spectrum-grey one). Note how background correction using a volatile-free glass could induce an overestimation of the height of the peak at 1515 cm^{-1} (black arrow), for high water contents.

Vetere et al., 2011). We performed the background correction in the 1000–2000 cm^{-1} region by manually subtracting a CO_2-free spectrum, with similar concentration of molecular H_2O scaled to the same thickness of the sample (as in Fig. 1), in order to minimise the error in the height estimation of the peak at 1515 cm^{-1}. We tested the influence of the extinction coefficient in the estimation of CO_2 concentration, by using extinction coefficients available in the literature for both carbonate bands and different mafic compositions. CO_2 contents in lamproitic to kamafugitic samples were calculated using extinction coefficients calibrated in basaltic, Ca-rich leucititic, and phonotephritic compositions: 375 cm^{-1} (Fine and Stolper, 1986), 355 cm^{-1} (Thibault and Holloway, 1994), 302 cm^{-1} (Behrens et al., 2009). The three different values are shown and compared in Table 3; the average value was used for data treatment. CO_2 contents in alkali-basalt samples were calculated using extinction coefficients calibrated in basaltic, basanitic and shoshonitic compositions: 375 cm^{-1} (Fine and Stolper, 1986), 398 cm^{-1} (Jendrzejewski et al., 1997), 281 and 284 cm^{-1} (Dixon and Pan, 1995) and 355 cm^{-1} (Vetere et al., 2011). Table 2 shows the average value and the standard deviation. Both for lamproitic-kamafugitic and alkali-basaltic compositions, observed variations are always within 20%.

An equation linking the density of the glass to its total water content was used in the computation of the amount of dissolved water. For the Etna composition the equation was experimentally calibrated by Lesne (2008): density (g/cm^3) = −0.0185 × wt% H_2O + 2.708. For the lamproitic to kamafugitic compositions we adopted the same equation

as it reasonably agrees with density measurements on K-rich melts (Behrens et al., 2009). The thickness of the doubly polished glass sections was measured with a Mitutoyo digital micrometre (accuracy ± 1 μm) and crosschecked with the microscope gear for every single measurement.

Partial pressures of H_2O and CO_2 were calculated from total pressures and dissolved water contents: H_2O pressure was initially calculated from the amount of H_2O dissolved in the melt, using the solubility law determined for pure water (Lesne et al., 2011a); then CO_2 pressure was obtained by subtracting H_2O pressure from total pressure. We estimate the error associated with this calculation to be less than 15%, the main contribution being the fit of the H_2O solubility data. The mole fraction of CO_2 in the fluid phase (in Table 2) was calculated as the ratio of total pressure and partial pressure of CO_2. We tested that the use of this method, in place of mass balance calculations or the weight-loss method (Shishkina et al., 2010) strongly reduces the scatter in the experimental data.

2.2. Results and comparison with existing data

Experimental results are listed in Table 2 for alkali-basaltic glasses and in Table 3 for lamproitic ones. All experimental glasses present homogeneous H_2O and CO_2 contents (Tables 2 and 3).

2.2.1. Etna composition

The data obtained using the Etna composition show that CO_2 solubility generally increases with CO_2 partial pressure (Fig. 2a) consistent with previous investigations (e.g. Stol-
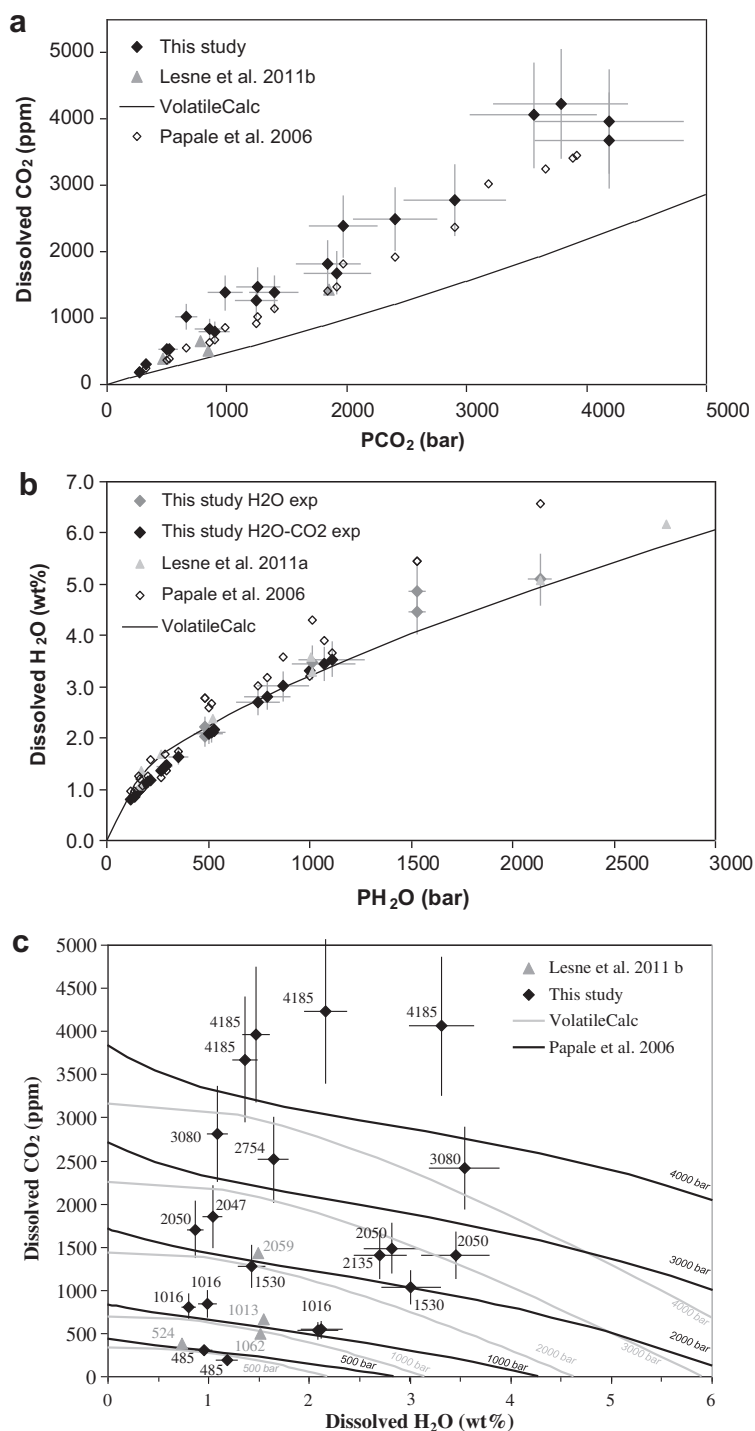
Fig. 2. Experimentally determined solubility of CO_2 and H_2O in the Etna basalt (data in Table 2), compared to theoretical solubilities calculated using Newman and Lowenstern (2002) (for $T = 1200$ °C and $SiO_2 = 47.95$ wt%) and Papale et al. (2006) (for $T = 1200$ °C and Etna composition in Table 1 with $Fe_2O_3 = 15\%$ of total FeO). (a) Dissolved CO_2 in ppm vs. partial pressure of CO_2 for our data and the data of Lesne et al. (2011b). X error bars are 20% of the mean value, in agreement with the maximum variation obtained using different extinction coefficients in CO_2 calculation (see Section 2.1). Y error bars show the maximum uncertainty that we estimate for P_{CO_2} calculation (15%). (b) Dissolved H_2O in wt% vs. partial pressure of H_2O for our data and the data of Lesne et al. (2011a). X error bars are 10% of the mean value, in agreement with the maximum standard deviation observed in FTIR measurements. Y error bars show the maximum uncertainty that we estimate for P_{H_2O} calculation (15%). (c) Dissolved H_2O in wt% vs. CO_2 in ppm for our data and the data of Lesne et al. (2011b). The number next to each experimental point indicates the experimental pressure. Experimental solubilities are compared with the isobaric solubilities calculated for total pressures of 500, 1000, 2000, 3000 and 4000 bar, as indicated on the graph. Error bars indicate the maximum analytical uncertainty of FTIR measurements: 10% for H_2O and 20% for CO_2.

per and Holloway, 1988; Thibault and Holloway, 1994; Jendrzejewski et al., 1997; Morizet et al., 2002; Botcharnikov et al., 2006; Lesne et al., 2011b). Fig. 2a and b also show the recently published data (Lesne et al., 2011a,b) for the same alkali-basaltic composition, our data extending the experimental conditions to higher pressure. This melt composition, although alkali-rich, is not far from those used for the calibration of existing models (Dixon, 1997; Newman and Lowenstern, 2002; Papale et al., 2006). When plotted in a P_{CO_2} vs. dissolved CO_2 plot (Fig. 2a) both our data and those of Lesne et al. (2011b) show a linear trend with a nearly 1:1 slope. Solubilities predicted by VolatileCalc (Newman and Lowenstern, 2002) and the model of Papale et al. (2006) at 1200 °C are also shown (Fig. 2a). In the first case, a solubility curve was calculated for 47.95 wt% SiO_2 at 1200 °C. In the second case, calculations have been performed on the website http://ctserver.ofm-research.org using (i) the Etna composition with $Fe^{3+}/Fe_{tot} = 0.15$ (in order to broadly reproduce the redox conditions during the experiments), (ii) experimental

pressures and temperature, and (iii) calculated CO_2 molar fractions in the fluid (Table 2). VolatileCalc underestimates CO_2 solubility by ∼45%. Values calculated using Papale et al. (2006) are in a good agreement with the experimental data, within the analytical error.

Fig. 2b shows our data for H_2O in a P_{H_2O} vs. dissolved wt% H_2O plot, compared to those of Lesne et al. (2011a) and calculations using the models of Papale et al. (2006) and VolatileCalc at 1200 °C. Although water was not loaded in some samples (those in which CO_2 was introduced as Ag_2CO_3), it was measured in the resulting glasses (Table 2 and Fig. 2b), probably due to (1) the presence of H_2O as an impurity in the gas pressure medium (Behrens, 2010), or (2) the presence of H_2 in the autoclaves, which reduces the ferric iron of the sample to ferrous iron and/or reduces ferrous iron to metal (iron loss in the capsule), thus generating H_2O (Gaillard et al., 2003). Despite this addition, water distribution in these samples is homogeneous, testifying that equilibrium conditions were reached during the experiments. Moreover, all our data are well aligned
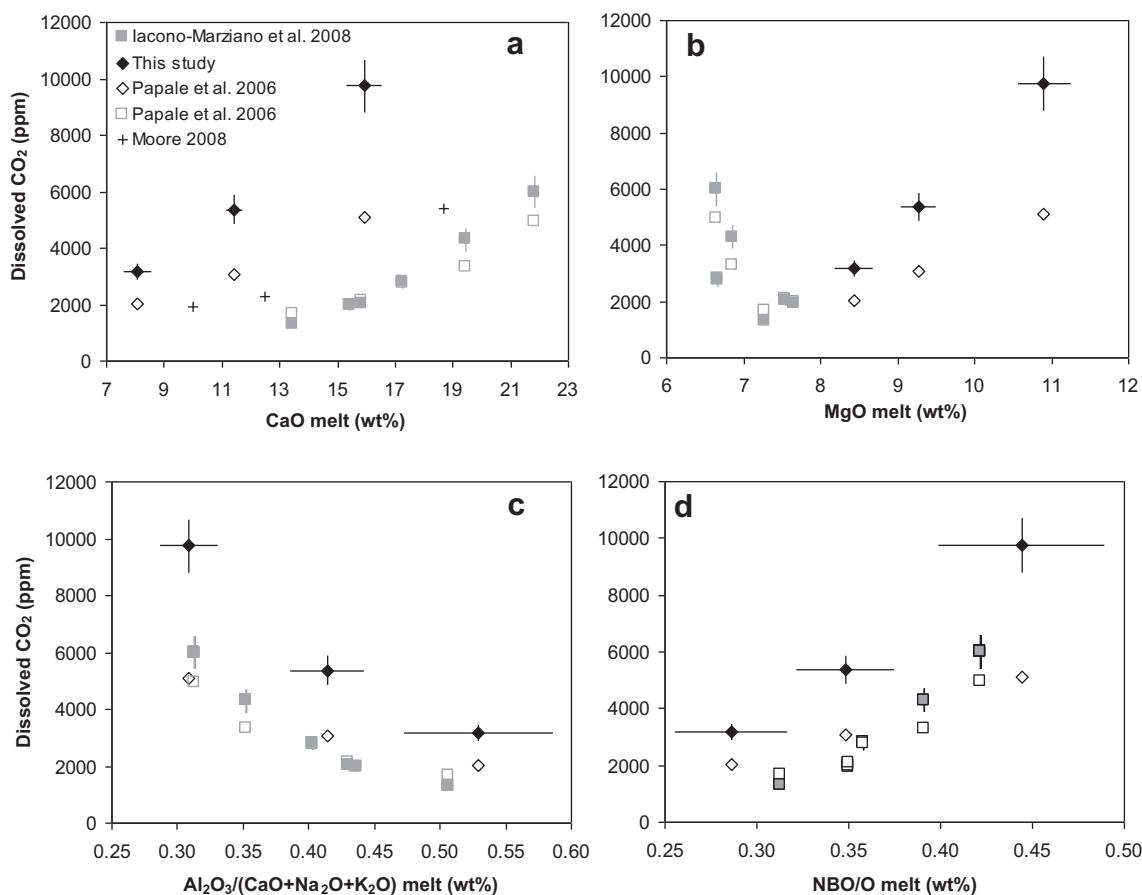

Fig. 3. Experimentally determined solubility of CO_2 in the lamproite-kamafugite melts. Data are in Table 3. (a) Dissolved CO_2 vs. CaO wt% content in the melt for our data and those of Iacono-Marziano et al. (2008). Data in calcic to calc-alkaline basalt composition containing 3–5 wt% H_2O (major element composition not available) obtained at 4000 bar and 1200 °C are also shown (Moore, 2008). For each experimental point of this study and Iacono-Marziano et al. (2008), solubilities calculated using Papale et al. (2006) are also shown (for $T = 1200$ °C and 2TA1, 2TA2 and 2TA3 compositions in Table 1 with $Fe_2O_3 = 15\%$ of total FeO). (b–d) Same experimental data points plotted against MgO, the agpatic index, and NBO/O, respectively. Y error bars indicate the analytical uncertainty of CO_2 measurements. X error bars show the standard deviation (2σ) of CaO and MgO EMP analysis (a and b) and the mathematically propagated measurement uncertainties for the agpaitic index and the NBO/O (c and d).

and consistent with CO_2-free data of Lesne et al. (2011a). Calculated solubility using VolatileCalc computed for 47.9 wt% SiO_2 is in good agreement with experimental data, while the model of Papale et al. (2006) (for Etna composition with Fe_2O_3 = 15% of total FeO) slightly overestimates experimental data at pressures higher than 500 bar.

When transposing in terms of total pressure (i.e. $P_{CO2} + P_{H2O}$), VolatileCalc significantly overestimates total pressures for given amounts of dissolved CO_2 and H_2O (Fig. 2c), e.g. when the experimental pressure is ~2000 bar, VolatileCalc calculates ~3000 bar for the same amount of H_2O and CO_2. The model of Papale et al. (2006) also overestimates, but to a lesser extent, total pressures up to 4000 bar (Fig. 2c).

2.2.2. Torre Alfina composition

CO_2 solubility data obtained at a single total pressure (3510 bar) with moderate variations of CO_2 fraction in the gas (75–96%) are shown in Fig. 3. Given that changes in the melt composition are essentially due to CaO and MgO addition, due to the use of Ca–Mg carbonates as the source of CO_2, we represent the data as dissolved CO_2 content vs. CaO or MgO in the melt (Fig. 3a and b, respectively). Experimental data for shoshonitic to Ca-rich shoshonitic compositions (Iacono-Marziano et al., 2008), obtained using a similar protocol (CO_2 added as Ca-carbonates), are also shown. Both trends suggest a strong control of the melt CaO content on CO_2 solubility (Fig. 3a) in potassic melts (this study), as in more sodic ones (Iacono-Marziano et al., 2008). This effect has already been observed in calcic to calc-alkaline basalt compositions (Moore, 2008), the experimental data being also shown in Fig. 3a. Melt compositions from the present study are substantially richer in alkalis than those from Iacono-Marziano et al. (2008), i.e. 7.6–9.1 wt% vs. 4.0–4.6 wt% $Na_2O + K_2O$, most likely justifying the shift in CO_2 solubility shown in Fig. 3a. Major element compositions are not indicated in Moore (2008). Our samples show an increase in CO_2 content from 3000 to 9000 ppm, with CaO contents increasing from 8 to 16 wt% (accompanied by a moderate increase in P_{CO2}: 2630 to 3370 bar). Solubilities calculated using the model of Papale et al. (2006) are also shown in Fig. 3a: while the data of Iacono-Marziano et al. (2008) are relatively well predicted (within 20%), our data for potassic compositions are underestimated by more than 50%. Therefore, although the model of Papale et al. (2006) predicts a strong effect of CaO content on CO_2 solubility (as also proposed by Dixon, 1997; Lesne et al., 2011b), our experimental data reveal that the magnitude of this effect needs to be recalibrated.

The effect of MgO contents of the melt is less clear (Fig. 3b), CO_2 solubility correlating positively with MgO in potassic melts (this study) and negatively in more sodic ones (Iacono-Marziano et al., 2008). The control of the melt alkali content on CO_2 solubility is difficult to verify by using these data, because variations in Na_2O and K_2O are very limited when compared to the variations in the CaO content.

We finally show how CO_2 solubility correlates with two structural parameters: (1) the agpaitic index, i.e. Al_2O_3/

($CaO + K_2O + Na_2O$), which has a strong effect on melt physical and structural properties (Mysen and Toplis, 2007) and (2) the NBO/O (non-bridging oxygen per oxygen), calculated on an anhydrous basis (see the Appendix). Both the agpaitic index and the NBO/O seem to be strongly correlated to CO_2 solubility, the former showing an inverse, while the latter a positive correlation with the amounts of CO_2 in the glasses (Fig. 3c and d).

3. MODEL

3.1. Database and global chemical trends

The database of H_2O–CO_2 solubility experiments is summarised in Table 4. We selected only experiments with mafic compositions, in which H_2O and CO_2 solubilities were simultaneously determined in order to model CO_2 solubility (182 experiments). In all experiments, except for those of Morizet et al. (2010), the mafic melts were equilibrated with H_2O–CO_2 fluids, in the absence of reduced species (e.g. CO, CH_4, H_2). In all selected experiments CO_2 is dissolved in the melt in the form of carbonates (CO_3^{2-}), as generally observed in mafic compositions. For H_2O solubility, we considered both pure H_2O solubility experiments (107 experiments) plus the H_2O–CO_2 experiments already taken into account in the CO_2 solubility model. Most of the experiments considered have been performed using internally heated pressure vessels (except those in Jakobsson, 1997; Métrich and Rutherford, 1998), which reduces database inconsistencies due to the use of different experimental setups. We restricted the pressure range to 1–10000 bar (1.0 GPa) for several reasons: (i) these pressures are the most interesting for volcanological purposes, (ii) experimental data at higher pressure are less numerous and most of them are not accompanied by required information about H_2O and CO_2 activities (Pan et al., 1991; Thibault and Holloway, 1994; Brooker et al., 2001a), (iii) we consider that above 10000 bar the fluid phase might not be considered as a mixture of perfect gases.

We selected only multi-component compositions, because we believe that mixing effects that could affect CO_2 solubility in simple systems would not necessarily operate in more complex systems with the same magnitude. Furthermore, although changes in composition in the selected database are important, they remain small in comparison to chemical changes that would be introduced by simplified synthetic systems (e.g. Al-free, alkali-free) and that would excessively influence the regression process.

Fig. 4a shows dissolved CO_2 contents vs. CO_2 pressure for each experimental work in Table 4. If not directly specified by the authors, CO_2 pressure was calculated from the total pressure and mole fraction of CO_2 in the fluid phase. In general, every given composition shows a nearly linear trend, whose slope strongly varies with the chemical composition of the melt. For clarity, Fig. 4b presents a selection of data that well illustrates how the trends vary for different melt compositions at low pressures (<2500 bar). In general, mid ocean ridge basalts (MORB) show the lowest CO_2 solubilities, while foiditic and tephritic melts display the highest ones. Calculated CO_2 solubilities at 1200 °C using the

Table 4
Database used in our calibration.

$n°$	Authors	Melt compositions (wt% SiO2)	Pressure range (bar)	Range of CO_2 contents (ppm)	Range of H_2O contents (wt%)
1	Hamilton et al. (1964)	Basalt (50.71)	3000–6067	–	5.93–9.40
		Andesite (58.41)	3000–5309	–	7.4–10.1
2	Stolper and Holloway (1988)	Basalt (50.92)	100–1531	27–549	0.06–0.65
3	Pawley et al. (1992)	MORB (49.46)	495–1503	103–901	0.01–3.00
4	Dixon et al. (1995)	MORB (50.8)	310–980	62–306	0.37–2.49
5	Moore et al. (1995)	Basalt-andesite (55.3)	1113–1930	–	3.67–5.06
		Andesite (62.6)	703–1865	–	2.62–5.03
		Augite-minette (53.6)	814–1280	–	3.41–4.55
6	Jakobsson (1997)	Na-Icelandite (54.55)	10000	10300–11900	1.22–8.69
7	Jendrzejewski et al. (1997)	MORB (52.0)	250–1950	126–960	0.27–0.62
8	Moore et al. (1998)	Basalt-andesite (55.3)	2896–3110	–	6.37–6.59
		Andesite (62.6)	2830–2985	–	6.76–6.82
		Basalt (50.6)	2117–2916	–	4.51–6.40
9	Métrich and Rutherford (1998)	Alkali basalt (46.7–48.28)	270–800	–	1.3–3.1
10	Berndt et al. (2002)	MORB (49.64)	505–5009	–	2.14–9.38
11	Botcharnikov et al. (2005)	Ferro-basalt (48.34)	2000	782–1061	0.72–2.90
12	Botcharnikov et al. (2006)	Andesite (57.44)	2000–5000	1010–4540	0.89–7.97
13	Di Matteo et al. (2006)	Shoshonite (51.8)	250–2000	–	1.01–4.40
		Latite (53.8)	520–2000	–	2.43–5.20
14	Iacono-Marziano et al. (2008)	Shoshonite to Ca-shosh. (50.26–45.04)	2130–2140	1300–6000	1.5–2.80
15	Behrens et al. (2009)	K-Foidite (49.89)	2000–5000	760–9150	0.87–9.27
16	Morizet et al. (2010)	Basalt (54.8)	1970–3300	514–1408	1.24–4.01
17	Shishkina et al. (2010)	Basalt (50.17)	500–5000	36–3334	0.1–6.68
18	Vetere et al. (2011)	Shoshonite (53.47)	500–4000	0–3080	0.64–7.92
19	Lesne et al. (2011a)	Alkali basalt (47.95)	172–3948	–	1.36–8.96
		Ca-rich basalt (49.40)	163–3948	–	0.98–8.47
		K-tephrite (48.02)	163–3948	–	1.08–8.23
20	Lesne et al. (2011b)	Alkali basalt (47.95)	269–2059	383–1429	0.73–1.55
		Ca-rich basalt (49.40)	269–2059	73–1170	0.71–1.58
		K-tephrite (48.02)	269–2059	215–2094	0.80–1.02
21	This study	Alkali basalt (47.95)	485–4185	170–3797	0.8–3.54
		K-lamproite to K-kama. (54.67–47.58)	3510	2913–8861	1.83–3.08

Most studies have been performed at 1200 °C, the entire T range is however 1100–1400 °C.

VolatileCalc model are also shown in Fig. 4 (a and b) for melt SiO_2 contents of 45, 47 and 49 wt%: they show that variations in melt silica content only do not satisfactorily explain the differences shown by experimental data (Table 4). For instance, the SiO_2 content of a MORB (~50–51 wt%) is only slightly higher than that of a foidite (49.89 wt%, Behrens et al., 2009), the highest CO_2 solubility in foiditic melts being most likely accounted for by their elevated K, Na, Ca contents.

The clearest deviations from linear trends in Fig. 4a (excluding the melts in Iacono-Marziano et al. (2008) that have variable compositions) are represented by experimental data obtained at high H_2O contents (Fig. 4c) and variable CO_2 activities (Jakobsson, 1997; Botcharnikov et al., 2006; Behrens et al., 2009; Shishkina et al., 2010). This could reflect the effect of water on CO_2 solubility, as already proposed by Mysen et al. (1975) and more recently by Behrens et al. (2009). When selecting the datasets with the largest ranges of dissolved water contents (Jakobsson, 1997; Behrens et al., 2009; Shishkina et al., 2010), a plot of the ratio of dissolved CO_2 to CO_2 partial pressure as a function of the bulk water content of the melt is consistent with an increase in CO_2 solubility with increasing water content in the melt (Fig. 5). Although the H_2O–CO_2 trends are shifted most likely due to the differences in melt composition (e.g. the total alkali content strongly decreases from the foiditic melt to the basaltic one) the three datasets show that the dissolution of 7–9 wt% H_2O enhances CO_2 solubility by a factor of 2–3. These trends may be partly explained by an overestimation of CO_3^{2-} contents in FTIR analyses of water-rich samples, due to the effect of the 1630 cm^{-1} band on the heights of the carbonate peaks (the high frequency one in particular, see Fig. 1). However, the importance of this effect should be very limited for the three studies (Jakobsson, 1997; Behrens et al., 2009; Shishkina et al., 2010), because the authors quantified CO_3^{2-} contents using the height of the low frequency peak of the doublet and calibrating its extinction coefficient. The trends in Fig. 5 cannot be explained by non-ideal mixing of H_2O and CO_2 in the fluid phase, because the Modified Redlich and Kwong models (Kerrick and Jacobs, 1981) predict a decreasing CO_2 fugacity coefficient with increasing H_2O fraction in the fluid, which should result in a decrease in melt CO_2 solubility (i.e. decrease of the ratio of dissolved carbonate in
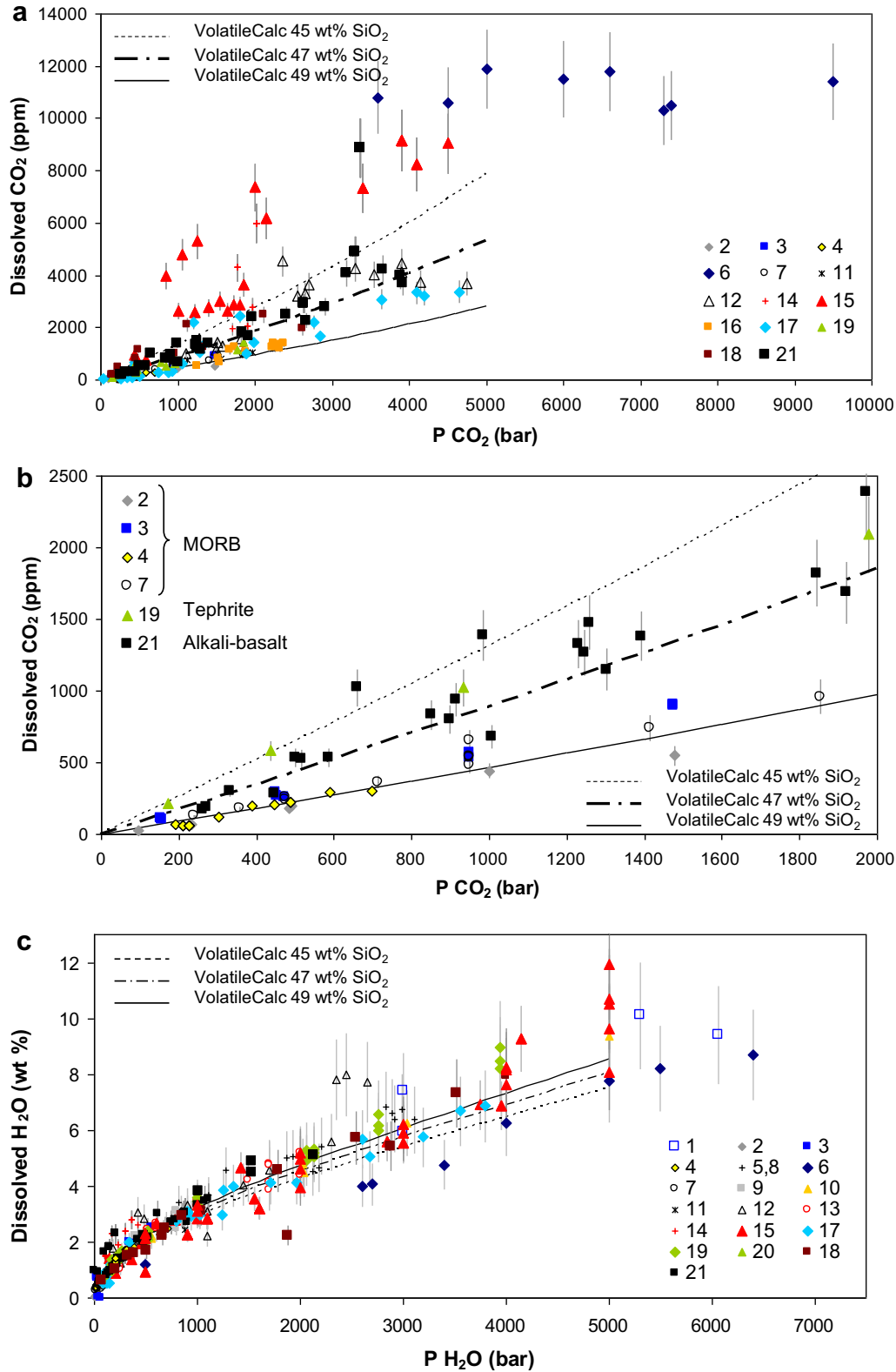
Fig. 4. H_2O–CO_2 solubility data for the experimental studies of Table 4 (numbers refer to the different studies listed in the table). Error bars indicate maximum uncertainties on CO_2 and H_2O measurements (20% and 10%, respectively). (a) Dissolved CO_2 (in ppm) vs. partial pressure of CO_2 for the 182 literature data. The solubility curves are calculated using Volatile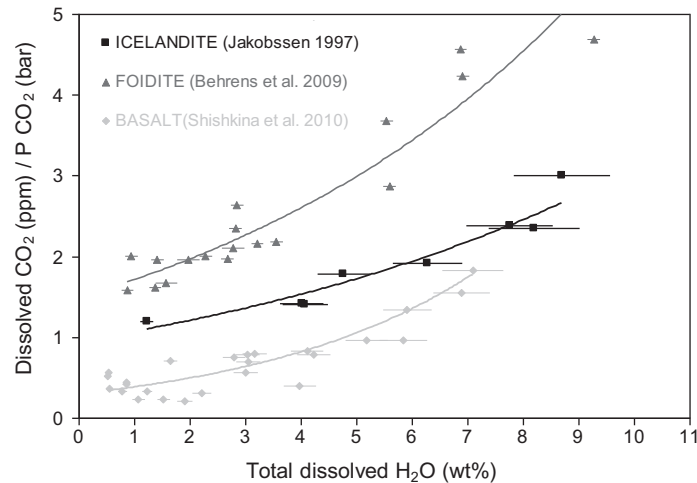Calc for basalts with SiO_2 contents of 45, 47 and 49 wt%. (b) Same plot as in (a) but on a restricted database. (c) Dissolved H_2O (in wt%) vs. partial pressure of H_2O for the 182 H_2O–CO_2 plus the 107 H_2O literature data. The solubility curves are calculated using VolatileCalc for basalts with SiO_2 contents of 45, 47 and 49 wt%.

Fig. 5. Dissolved CO_2 content in ppm normalised to the CO_2 partial pressure vs. dissolved water content for three sets of data indicated in the legend. Error bars show the standard deviation (2σ) associated to every H_2O measurement. The experimental data show increasing CO_2 solubility with increasing water content in the three mafic melts with different compositions indicated in the legend.

the melt to CO_2 partial pressure in the fluid) with increasing water content. This is in total disagreement with experimental observations.

In order to appreciate the variation of CO_2 solubility with CO_2 partial pressure, independently of the effect of H_2O, data with similar amounts of dissolved water and variable CO_2 contents have been selected. Fig. 6a shows that for a given H_2O content, CO_2 solubility in three substantially different compositions has a clear linear relationship with CO_2 partial pressure, up to 5000 bar total pressure. Over a similar pressure range, on the contrary, CO_2 fugacity (at 1200 °C) is calculated to exponentially increase with pressure (Fig. 6a). The different trends of CO_2 solubility are most likely due to increasing total alkali content from the MORB composition to the foiditic one and to the different water contents of the three datasets. Moreover, Fig. 6b illustrates how, for a given melt composition, i.e. MORB (data from Shishkina et al., 2010), CO_2 solubility increases with increasing H_2O dissolved in the melt.

Fig. 4c shows dissolved H_2O contents vs. H_2O pressure for each experimental work in Table 4. As in Fig. 4a, H_2O solubilities calculated at 1200 °C for melt SiO_2 contents of 45, 47 and 49 wt% using VolatileCalc are also shown. Experimental data for H_2O (Fig. 4b) show a more limited scatter than those for CO_2 (Fig. 4a). Calculated H_2O solubilities (using VolatileCalc) also show more limited variations with the SiO_2 content of the melt than CO_2 ones. Therefore, it seems difficult to assess any chemical control on water solubility in mafic melts, as underlined by earlier works (Moore et al., 1998; Lesne et al., 2011a).

3.2. Structural and thermodynamic background and operated simplifications

3.2.1. CO_2 solubility

In andesitic to ultramafic melt compositions, CO_2 is soluble as carbonate groups (Fine and Stolper, 1986) after the reaction with oxygen anions:

$$CO_2^{(fluid)} + O^{2-(melt)} \rightarrow CO_3^{2-(melt)} \tag{1}$$
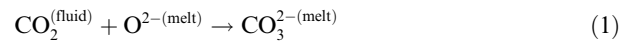
The Mass Action Law allows us to write the thermodynamic constant K_c of Eq. (1) as:

$$\mathrm{Ln}K_C^{(P,T)} = \mathrm{Ln}\frac{a_{CO_3^{2-}}}{f_{CO_2} \times a_{O^{2-}}} = \mathrm{Ln}\frac{\gamma_{CO_3^{2-}} \times X_{CO_3^{2-}}}{f_{CO_2} \times a_{O^{2-}}} \tag{2}$$

where a is the component activity, f its fugacity, X its molar fraction and γ its activity coefficient. The thermodynamic constant K_c can be expressed as a function of pressure (P), and temperature (T) as:

$$\mathrm{Ln}K_C^{(P,T)} = -\left(\frac{\Delta G^\circ}{R \times T}\right) = -\left(\frac{\Delta H^\circ}{R \times T} - \frac{\Delta S^\circ}{R} + \frac{P\Delta V^\circ}{R \times T}\right) \tag{3}$$

ΔG°, ΔH°, ΔS° and ΔV° respectively refer to the Gibbs free energy, enthalpy, entropy and volume changes of equilibrium (1) calculated considering components in their standard states at P and T of interest. R is the gas constant. Combination of (2) and (3) yields:

$$\mathrm{Ln}\left(X_{CO_3^{2-}}\right) = -\mathrm{Ln}\left(\gamma_{CO_3^{2-}}\right) + \mathrm{Ln}(f_{CO_2}) + \mathrm{Ln}(a_{O^{2-}})$$
$$- \left(\frac{\Delta H^\circ}{R \times T} - \frac{\Delta S^\circ}{R} + \frac{P\Delta V^\circ}{R \times T}\right) \tag{4}$$

The formalism that we adopt is an empirical equation inspired by Eq. (4), to which we apply several important simplifications. The fraction of carbonate ($X_{CO_3^{2-}}$) is rescaled to its concentration in ppm $[CO_3^{2-}]^{ppm}$, which is a convenient unit to compare with solubility measurements (as frequently done for models of volatile solubility, i.e. sulphur solubility see O'Neill and Mavrogenes, 2002). Moreover, we assume that the activity coefficient for dissolved carbonate groups ($\gamma_{CO_3^{2-}}$) is a linear function of chemical–structural parameters and we introduce an empirical expression of the dependence of carbonate group activity coefficients to the melt chemical compositions as:

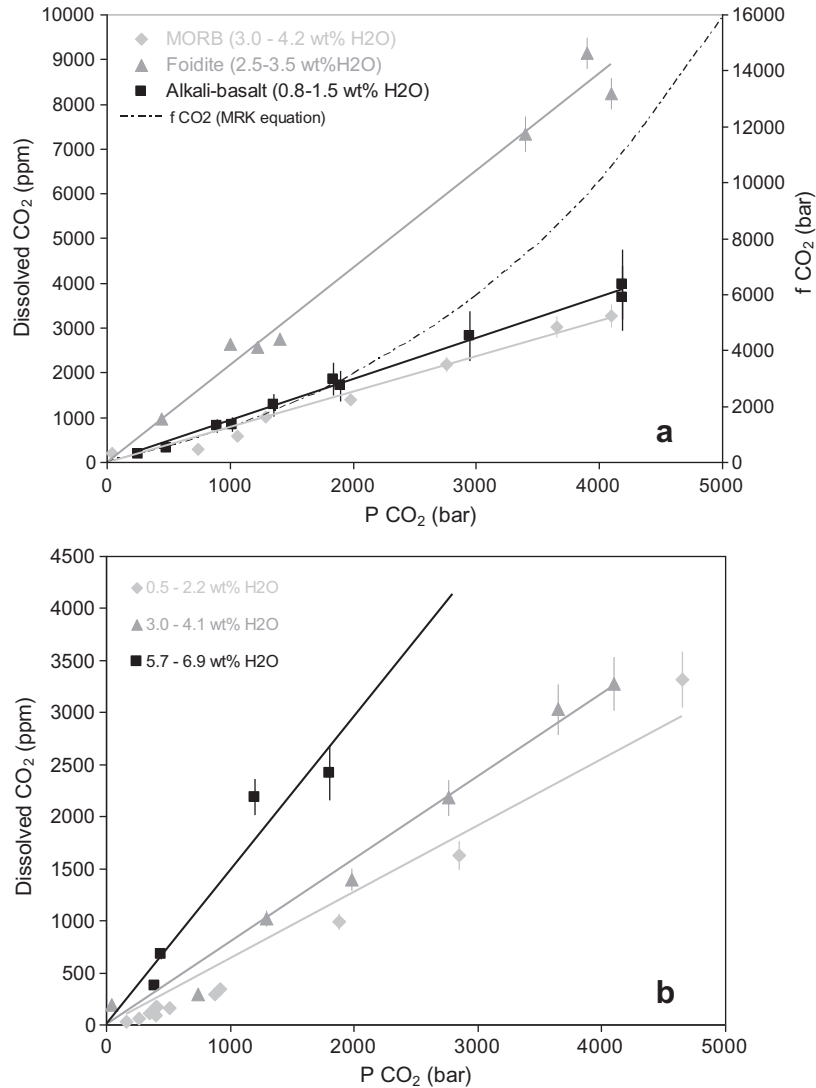$$-\mathrm{Ln}\left(\gamma_{CO_3^{2-}}\right) = \sum_1^i x_i \times d_i \tag{5}$$

Fig. 6. Dissolved CO_2 content in ppm as a function of CO_2 partial pressure for different sets of data with a relatively constant water content indicated in the legend. Error bars indicate the standard deviation (2σ) reported by the authors for every CO_2 measurement. (a) Three substantially different melt compositions and water contents: foidite with 2.5–3.5 wt% H_2O (Behrens et al., 2009), MORB with 3–4 wt% H_2O (Shishkina et al., 2010), and alkali-basalt with 0.8–1.5 wt% H_2O (this study). The increase in CO_2 fugacity (calculated with a Modified Redlich Kwong equation) with increasing CO_2 partial pressure is also shown. (b) Three different ranges of H_2O contents for the same MORB composition (Shishkina et al., 2010).

where the d_i terms express the chemical control of selected oxides or ratio of oxides (x_i) on CO_2 solubility. This sort of simplification has also been used for sulphur solubility in silicate melts (Wallace and Carmichael, 1992). We stress that in conventional Margules mixing formalisms, the activity coefficient is also expressed as an exponential function of the component molar fractions.

We also assume that:

$$\mathrm{Ln}\left(a_O^{2-}\right) = b \times \left(\frac{\mathrm{NBO}}{\mathrm{O}}\right) \qquad (6)$$

where NBO/O, non-bridging oxygen divided by oxygen, is considered here as a measure of the activity of oxygen anions: it expresses the availability of oxygen in the melt to form carbonate groups. In choosing this parameter we took

into account that CO_2 solubility is recognised to be a strong function of NBO by spectroscopic and theoretical investigations (Brooker et al., 2001a,b; Guillot and Sator, 2011). Assessing the effect of H_2O on the concentration of NBO in mafic magmas is rather difficult, as no systematic quantitative studies have been conducted on complex depolymerised melts. We therefore tested two opposite scenarios, by calculating NBO/O on both anhydrous (according to Marrocchi and Toplis, 2005) and hydrous basis (see the Appendix for the details of the calculation). In the latter case, we made the assumption that the formation of NBO is induced by the dissolution of OH groups into the melt (Zotov and Keppler, 1998; Xue and Kanzaki, 2004). Xue and Kanzaki (2004) suggest that only 60% of the OH dissolved in CaO–MgO–SiO$_2$ without Al contributes to

NBO formation. However, in the absence of systematic studies of NBO creation due to water dissolution in different melt compositions, we preferred to test the most extreme case in which all the OH groups produce NBO.

Finally, by assuming that the enthalpy, entropy and volume terms of equilibrium (1) are not varying significantly with intensive P and T, we propose the following expression:

$$Ln\left[CO_3^{2-}\right]^{ppm} = \sum_1^i x_i \times d_i + a \times Ln[P_{CO_2}] + b \times \left[\frac{NBO}{O}\right] + \frac{A}{T} + B + C \times \frac{P}{T} \quad (7)$$

where the terms a, b, A, B and C are adjusted parameters, together with the d_i terms.

In the chemical contribution to the activity coefficient of CO_3^{2-} (Eq. (5)), we have tested the effects of 8 major melt oxides, i.e. SiO_2, Al_2O_3, FeO, MgO, CaO, Na_2O, K_2O, H_2O, and of the agpaitic index that expresses CO_3^{2-} affinity for different cations and the charge balancing or network modifying effect of cations.

Adjusting the effect of water on CO_2 solubility is difficult because, from a statistical point of view, both parameters do not vary independently in the considered database (i.e. in most experiments considered, X_{CO2} is estimated using the relationship $P_{CO2} + P_{H2O} = P_{total}$) and because mixing properties in the H_2O–CO_2 fluid, which are ignored here, may well affect the solubility of H_2O–CO_2 in melt without requiring any interaction between dissolved water and dissolved CO_2. But we recall that fluid mixing properties as calculated using available equations cannot explain the effect of increasing water content on CO_2 solubility (Fig. 5). In Eq. (7), we therefore introduced a parameter (d_{H2O}) that accounts for the effect of water.

We used CO_2 partial pressure (P_{CO2}) rather than fugacity (f_{CO2}); this is a convenient simplification that (i) is justified by experimental data showing linear correlation between CO_2 solubility and CO_2 partial pressure (Figs. 2a and 6) and (ii) does not weaken the model results since we tested that the use of CO_2 fugacity instead of CO_2 partial pressure does not yield a better fit than CO_2 pressure. Furthermore, the value of the parameter a, which expresses the deviation of the CO_2 activity or fugacity in the gas with respect to P_{CO2}, is shown later (Section 3.3) to justify this simplification.

The term b defines how CO_2 solubility depends on NBO/O. A, B, C represent respectively the enthalpy, entropy and volume changes of expressed in Eq. (4): $\frac{\Delta H°}{R}$, $\frac{\Delta S°}{R}$, $\frac{\Delta V°}{R}$ expressed in J/ppm CO_3^{2-}. The signs of these three parameters are set positive, and after the fitting, they come out positive or negative depending on how the adjusted parameters correlate with CO_2 solubility.

3.2.2. H_2O solubility

Regarding water solubility in mafic melts, the general solubilisation reactions are written as follows (Stolper, 1982):

$$H_2O^{(fluid)} \rightarrow H_2O^{(melt)} \quad (8)$$

$$H_2O^{(melt)} + O^{2-(melt)} \rightarrow 2OH^{-(melt)} \quad (9)$$
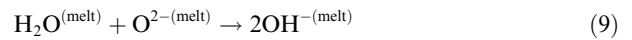
The stochiometry of reaction (8) implies that water solubility is a square root function of water fugacity:

$$LnK_H^{(P,T)} = Ln\frac{a_{OH^-}^2}{f_{H2O} \times a_{O^{2-}}} = Ln\frac{(\gamma_{OH^-} \times X_{OH^-})^2}{f_{H2O} \times a_{O^{2-}}} \quad (10)$$

By using the same empirical formalism as Eqs. (5)–(7), we consider:

$$Ln[H_2O]^{wt\%} = \sum_1^i x_i \times d_i + a \times Ln[P_{H2O}] + b \times \left[\frac{NBO}{O}\right] + \frac{A}{T} + B + C \times \frac{P}{T} \quad (11)$$

3.3. Model calibration

The best fits for CO_2 and H_2O using Eqs. (7) and (11), respectively, are obtained using the parameters listed in Tables 5 and 6, which were adjusted using classical linear fitting procedures, which minimise residuals between measured and calculated solubilities using Eqs. (7) and (11). All parameters of Eqs. (7) and (11) are simultaneously solved. The regression parameters were retained or removed, on the basis of the relative uncertainty ascribed by the fitting routine and their ability to significantly improve the fit (more than 10% on the residue). In our database NBO/O varies between 0.15 (the latite of Di Matteo et al., 2006) and 0.45 (sample TA3 in this study), on an anhydrous basis, and between 0.18 (the andesite of Moore et al., 1995) and 0.64 (the foidite in Behrens et al., 2009), on a hydrous basis. In both cases, NBO/O is the chief factor in controlling CO_2 solubility, the type of the modifier cation bonded to NBO also having a crucial role (see Section 3.6). As explained in Section 3.2, we tested two different versions

Table 5
Adjusted parameters and their standard errors for CO_2 solubility in mafic melts.

	d_{H2O}	$d_{Al2O3/(CaO+K2O+Na2O)}$	$d_{FeO+MgO}$	$d_{Na2O+K2O}$	a_{CO2}	b_{CO2}	C_{CO2}	B_{CO2}
Hydrous	–16.4	4.4	–17.1	22.8	1.00	17.3	0.12	–6.0
St. error (2σ)	1.2	0.4	0.9	1.1	0.03	0.9	0.02	0.4
Anhydrous	2.3	3.8	–16.3	20.1	1.00	15.8	0.14	–5.3
St. error (2σ)	0.5	0.4	0.9	1.1	0.03	0.9	0.02	0.4

Adjusted parameters to calculate CO_2 solubility from Eq. (12) in the text. Two sets of parameters were calibrated from the experimental database in Table 4, employing NBO calculated on both a hydrous and anhydrous basis. Species concentrations (x_i) are in mole fraction, P and T are in bar and Kelvin respectively. R^2 of the regression is 0.98, for both models and the average error is 13% for the model with NBO calculated on a hydrous basis, and 14% for the model with NBO calculated on an anhydrous basis.

Table 6
Adjusted parameters and their standard errors for H_2O solubility in mafic melts.

	a_{H2O}	b_{H2O}	B_{H2O}	C_{H2O}
Hydrous	0.53	2.35	−3.37	−0.02
St. error (2σ)	0.02	0.28	0.13	0.02
Anhydrous	0.54	1.24	−2.95	0.02
St. error (2σ)	0.02	0.33	0.17	0.02

Adjusted parameters to calculate H_2O solubility from Eq. (13) in the text. Two sets of parameters were calibrated from the experimental database in Table 4, employing NBO calculated on both a hydrous and anhydrous basis. P and T are in bar and Kelvin respectively. R^2 of the regression = 0.91, Average error = 17% for the model with NBO calculated on a hydrous basis, while $R^2 = 0.85$, Average error = 21% for the model with NBO calculated on an anhydrous basis.

of our model, the former employing NBO calculated on an anhydrous basis and the latter using NBO calculated on a hydrous basis: adjusted parameters were calibrated for both scenarios and are reported in Tables 5 and 6.

Adjusted parameters to calculate CO_2 solubility differ only modestly between the two formalisms, the most critically affected being the coefficient expressing CO_2 solubility dependence on water content (Table 5). With NBO calculated on a dry basis, d_{H2O} is positive indicating that water incorporation increases CO_2 solubility. When NBO is calculated on a hydrous basis, the negative d_{H2O} does not imply that water decreases CO_2 solubility. In fact for this model, water incorporation increases NBO/O which then translates into an increase in CO_2 solubility. The impact of water on NBO/O dominates over the negative coefficient d_{H2O}, similarly to Fe and Mg (see Section 3.6). Later in this section we show how the version of the model that employs NBO calculated on a hydrous basis gives more relevant results for CO_2-poor, H_2O-rich melts.

We tested the relevance of d_i terms for SiO_2, Al_2O_3 and CaO but none of these improve the fit and they were therefore removed. Indeed the effect of calcium and aluminium oxides is much better fitted when treated as agpaitic index (i.e. Al/(Ca + K + Na)) rather than using Al_2O_3 and CaO as independent parameters. The effects of K_2O and Na_2O were found to be identical within their uncertainties: we therefore merged them into one parameter ($d_{K2O+Na2O}$). Similarly, MgO and FeO have comparable effects on CO_2

solubility, which is accounted for by a single parameter ($d_{MgO+FeO}$).

The parameter a was introduced to account for possible deviation from ideal behaviour of the CO_2–H_2O gas mixture that would impact on CO_2 solubility: its fitted value is 1.00 ± 0.03 for both versions of the model (Table 5), clearly indicates that using P_{CO_2} instead of f_{CO_2} is a useful and justified simplification.

The parameter A in Eq. (7) was eliminated because the fitted value was close to zero and its associated error was larger than the parameter itself. This is probably due to the relatively small temperature range of the experimental database (1100–1400 °C), and may also imply a limited temperature effect on CO_2 solubility in mafic melts as revealed by Pan et al. (1991) and discussed by Guillot and Sator (2011) based on theoretical grounds. Our model still predicts a weak inverse temperature dependence of CO_2 solubility, due to the term $C \times P/T$ in Eq. (7).

The correlation among model parameters for CO_2 solubility is shown in Table 7. Several parameters are correlated, mainly because the mole fractions of oxide components used in the compositionally dependent activity coefficient terms (Eq. (5)) are also employed to calculate NBO/O and the agpaitic index (AI). In particular, NBO/O and AI are highly correlated, we however selected both parameters because (i) their structural meaning is different, as specified above, and (ii) they both strongly improve fitting results.

For water solubility, it appears that the d_i terms that were used for CO_2 are unjustified from a statistical point of view: H_2O solubility seems poorly sensitive to the melt chemical compositions as found in earlier studies (Moore et al., 1998; Lesne et al., 2011a). We therefore adopted the simplest formulation possible by ignoring any chemical control on water solubility. Like for CO_2, fugacity does not improve the fitting with respect to pressure: a value of $a \cong 0.5$ (Table 6) reflects the classical observation of a square root relationship between water solubility and water activity (see Burnham and Davis, 1971 or more recently Shishkina et al., 2010). Similarly to CO_2, the parameter A in Eq. (11) was eliminated because the fitted value was close to zero and its associated error was larger than the parameter itself. Only NBO/O has been considered in addition to a constant and a P/T term. The parameters determined using NBO calculated on both a hydrous and an anhydrous basis are in Table 6. The differences between the two ver-

Table 7
Correlation coefficients among model parameters used for CO_2 solubility.

	P/T	$Ln[P_{CO2}]$	NBO/O anhydr.	NBO/O hydr.	$Na_2O + K_2O$	FeO + MgO	AI	H_2O
P/T	1	0.76	−0.26	0.25	0.27	−0.55	0.12	0.66
Ln (P_{CO2})	0.76	1	−0.05	0.11	0.22	−0.38	−0.06	0.22
NBO/O anhydr.			1	–	0.04	0.54	−0.91	−0.33
NBO/O hydr	0.25	0.11	–	1	0.20	0.04	−0.71	0.46
$Na_2O + K_2O$	0.27	0.22	0.04	0.20	1	−0.32	−0.30	0.23
FeO + MgO	−0.55	−0.38	0.54	0.04	−0.32	1	−0.24	−0.62
AI	0.12	−0.06	−0.91	−0.71	−0.30	−0.24	1	0.19
H_2O	0.66	0.22	−0.33	0.46	0.23	−0.62	0.19	1

AI: $Al_2O_3/(CaO + K_2O + Na_2O)$.

sions of the model are small both for CO_2 and H_2O, however when NBO/O is calculated on a hydrous basis the fit of experimental data is slightly improved: R^2 of the regression is 0.98 for CO_2 and 0.91 for H_2O and the average error is 13% for CO_2 and 17% for H_2O (the version employing NBO/O calculated on an anhydrous basis has $R^2 = 0.98$

for CO_2 and 0.85 for H_2O and average error = 14% for CO_2 and 21% for H_2O).

We tested the two versions (employing NBO calculated on a hydrous and on an anhydrous basis) of our model for CO_2 (Eq. (7)) on H_2O–CO_2 solubility in the Etna alkali-basaltic melt (Table 1). Fig. 7a shows the different
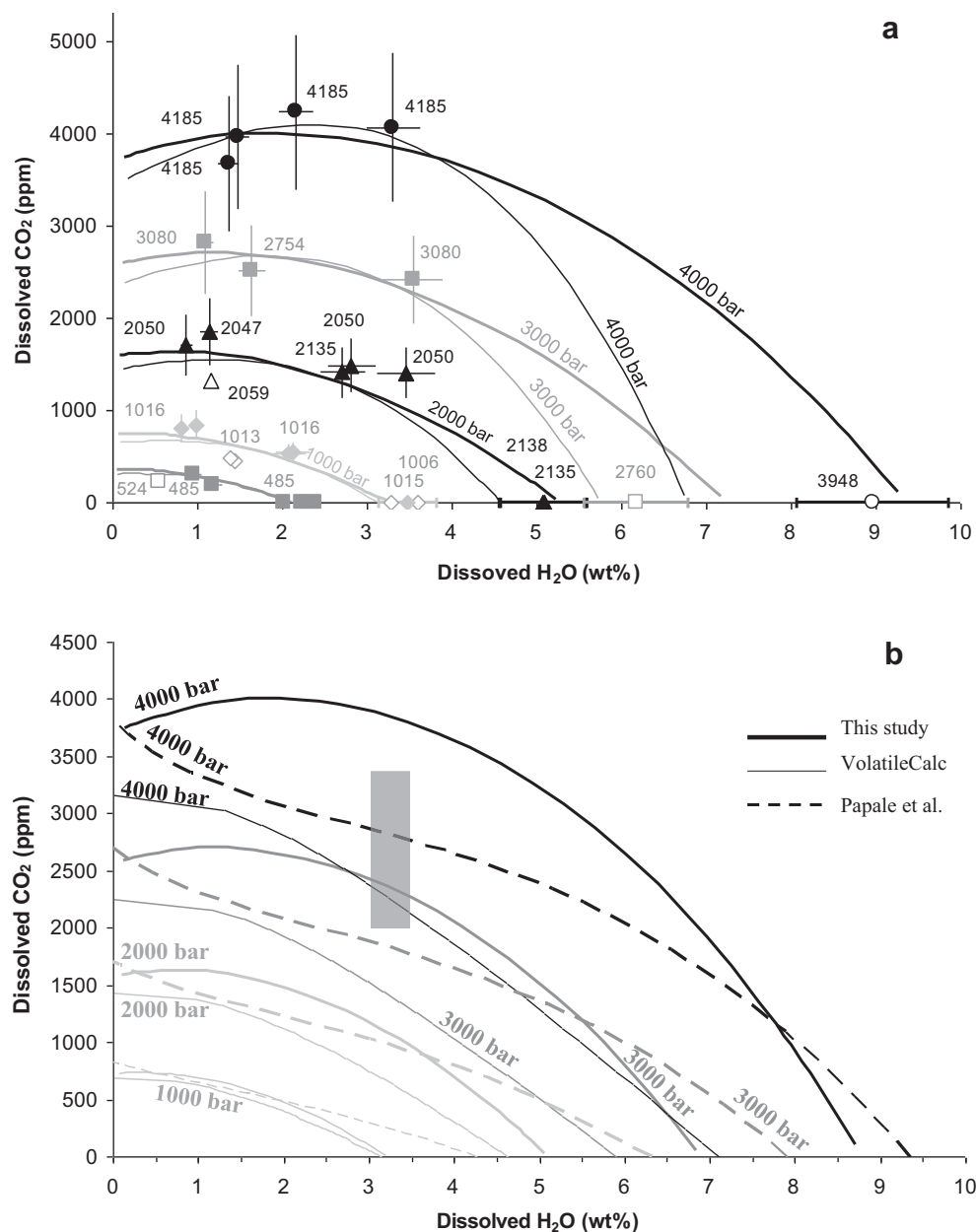
Fig. 7. H_2O–CO_2 solubilities calculated for the Etna composition (in Table 1). (a) Isobaric curves for total pressure between 500 and 4000 bar, calculated using the two versions of our model: thick lines show calculations employing NBO computed on a hydrous basis (and using the parameters in the first line of Table 5); thin lines show calculations employing NBO computed on an anhydrous basis (and using the parameters in the third line of Table 5). The points show experimental data: closed symbols represent data from this study, while open symbols indicate data from Lesne et al. (2011a,b). Error bars indicate the analytical uncertainty of FTIR measurements. (b) Comparison between isobaric curves (for 1000, 2000, 3000 and 4000 bar) computed using our model (employing NBO calculated on a hydrous basis), the model of Newman and Lowenstern (2002) (for $T = 1200$ °C and $SiO_2 = 47.95$ wt%) and the model of Papale et al., 2006 (for $T = 1200$ °C and Etna composition in Table 1 with $Fe_2O_3 = 15\%$ of total FeO). The grey box represents H_2O–CO_2 contents of primitive melt inclusions from Etna (Spilliaert et al., 2006).

shapes of H_2O–CO_2 isobaric curves between 500 and 4000 bar calculated using the two sets of parameters in Table 5. Larger differences are observed for H_2O contents higher than 4 wt%, due to the lack of experimental data. However, pure H_2O data that were not used for the calibration of the CO_2 model strongly suggest that the use of NBO, when calculated on a hydrous basis, allows to better estimate CO_2 solubility at high H_2O contents. We will therefore use this version of the model for the following discussions.

When compared with VolatileCalc and the model of Papale et al. (2006) for the Etna composition at 1200 °C (Fig. 7b), our model shows several significant differences. Substantial divergence exists between our model and VolatileCalc at pressures $\geqslant 2000$ bar, for instance, for similar H_2O–CO_2 contents (between 2 wt% H_2O-3000 ppm CO_2 and 7 wt% H_2O-0 ppm CO_2), our model predicts 3000 bar of total pressure while VolatileCalc 4000 bar. The divergences with the model of Papale et al. (2006) are also important for water content in the range 0–6 wt% and for total pressure equivalent or higher than 3000 bar. These variations between models are crucial when interpreting H_2O–CO_2 contents in melt inclusions in terms of entrapment depths. In case of Mt. Etna, for example, Spilliaert et al. (2006) reported a group of primitive melt inclusions with H_2O and CO_2 content of 3–3.5 wt% and 2000–3500 ppm, respectively. Such volatile contents define a field (grey box in Fig. 7b) where the discrepancies among models are the highest. The main source of discrepancy between our model and the others is the treatment of the effect of water on CO_2 solubility. The positive effect of H_2O on CO_2 solubility that we consider results in the bell-shape relationship shown in Fig. 7, whose curvature increases with pressure. However, experimental data are rare for high water contents at pressure exceeding 5000 bar and do not allow us to robustly calibrate this effect at high pressure.

3.4. Model results

The final model equations for CO_2 and H_2O solubility resulting after operated simplifications are therefore:

$$\begin{aligned} Ln[CO_3^{2-}]^{ppm} = &(x_{H2O} \times d_{H2O} + x_{AI} \times d_{AI} + x_{FeO+MgO} \\ &\times d_{FeO+MgO} + x_{Na2O+K2O} \times d_{Na2O+K2O}) \\ &+ a_{CO2} \times Ln[P_{CO_2}] + b_{CO2} \times \left[\frac{NBO}{O}\right] \\ &+ B_{CO2} + C_{CO2} \times \frac{P}{T} \end{aligned} \quad (12)$$

$$\begin{aligned} Ln[H_2O]^{wt\%} = &a_{H2O} \times Ln[P_{H_2O}] + b_{H2O} \times \left[\frac{NBO}{O}\right] \\ &+ B_{H2O} + C_{H2O} \times \frac{P}{T} \end{aligned} \quad (13)$$

where d_{H2O}, d_{AI} (with $AI = Al_2O_3/(CaO + K_2O + Na_2O)$), $d_{FeO+MgO}$, $d_{Na2O+K2O}$, a_{CO2}, b_{CO2}, B_{CO2}, C_{CO2} are the adjusted parameters listed in Table 5. a_{H2O}, b_{H2O}, B_{H2O}, C_{H2O} are the parameter listed in Table 6. x_{H2O} is the molar fraction of water in the melt, x_{AI} is the agpaitic index calculated as the ratio of the molar fraction of Al_2O_3 and the sum of the molar factions of CaO, K_2O and Na_2O in the

melt, $x_{FeO+MgO}$, $x_{Na2O+K2O}$ are the sum of the molar fractions of FeO and MgO and of Na_2O and K_2O in the melt, respectively. P is the total pressure in bar and T is the temperature in K. P_{CO2} and P_{H2O} are the partial pressures in bar of CO_2 and H_2O, respectively.

Fig. 8 (a–c) shows CO_2 and H_2O solubilities calculated using our model employing NBO calculated on a hydrous basis vs. measured solubilities from the database in Table 4. For CO_2 (Fig 8a and b), the regression coefficient is 0.98 and we calculate an average error of 13% (see the Appendix). The fitting for water solubility is of lower quality than that for CO_2 (Fig. 8c), i.e. the regression coefficient is 0.91 and we calculated an average error of 17% (see the Appendix).

A web application of the model is available at the following address: https://www.calcul.isto.cnrs-orleans.fr/apps/h2o-co2-systems/. An obvious "mathematical" limitation of the model is that it cannot calculate for $P_{CO2} = 0$, $P_{H2O} = 0$, $CO_2 = 0$ and $H_2O = 0$, due to the occurrence of the terms $Ln[P_{CO2}]$, $Ln[P_{H2O}]$, $Ln[CO_3^{2-}]$, and $Ln[H_2O]$ in Eqs. (12) and (13). The web application therefore considers that CO_2 and H_2O solubilities are zero for P_{CO2} and $P_{H2O} = 0$, respectively, and that P_{CO2} and $P_{H2O} = 0$, for $[CO_3^{2-}]^{ppm}$ and $[H_2O]^{wt\%} = 0$, respectively.

3.5. Model limitations

In this paragraph, we analyse the five weakest points of our modelling, which, in fact, derive from the limitations of the existing experimental database. (1) The effect of MgO and FeO on CO_2 solubility is still poorly experimentally constrained: most of the data present limited variations in these two oxides and in particular in MgO (mainly between 6 and 8 wt%); moreover, data for ultramafic compositions are missing. (2) The effect of K_2O replacement by Na_2O on CO_2 solubility is also poorly constrained: several systematic studies exist at variable pressure for K_2O-rich melts (Behrens et al., 2009; Lesne et al., 2011b; this study), but not for Na-rich melts (only Jakobsson, 1997 at 1 GPa). (3) The temperature effect on H_2O–CO_2 solubility has not been evaluated, because the variations in experimental temperatures are very limited: most of the data have been produced between 1200 and 1300 °C, the whole temperature range varying between 1100 and 1400 °C. (4) The possible contrasting roles of molecular H_2O and hydroxyl on melt structure (the number of NBO in particular), and the associated consequences for CO_2 solubility (i.e. how these hydrous species are distributed relatively to carbonate groups) needs to be further investigated by dedicated experimental studies. (5) We ignored in our treatment the possibility that ferrous and ferric iron may have different effects on CO_2 solubility; all iron is treated as ferrous iron and we obtained a regressed parameter for FeO that is similar to the one for MgO. In the mixing formalism used in Papale et al. (2006), FeO and Fe_2O_3 melt oxides have drastically differing effects on CO_2 solubility. Iron is recognised to exhibit different structural behaviour as a function of its oxidation state. Brooker et al. (2001b) showed that CO_3^{2-} environments have a changing configuration when Fe is switched between 3+ and 2+. Hence, we may expect CO_2
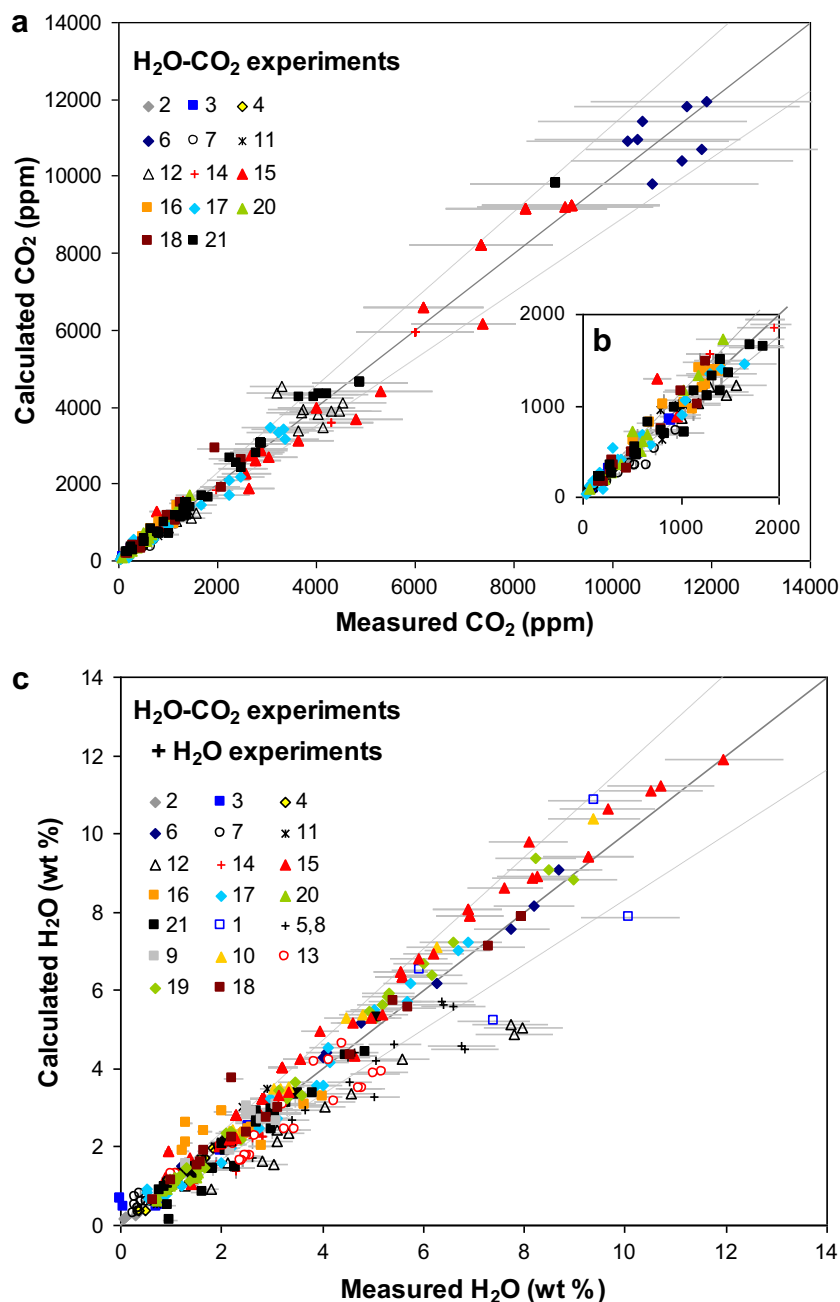
Fig. 8. Test of our model (Eqs. (7) and (11), with parameters in Tables 5 and 6) on the entire database (numbers refer to the different studies listed in Table 4). (a) Calculated vs. experimentally determined CO_2 solubility. Error bars show an error of 20% for measured CO_2 contents, which represent the maximum uncertainty for CO_2 determination by FTIR spectroscopy. The model error for calculated CO_2 contents (13%) is indicated by the discontinuous lines. (b) Calculated vs. experimentally determined H_2O solubility. Error bars show an error of 10% for measured H_2O contents, which represent the maximum uncertainty for H_2O determination by FTIR spectroscopy. The model error for calculated CO_2 contents (17%) is indicated by the discontinuous lines. The scatter in calculated vs. measured water content reflects the scatter of experimental data (Fig. 4c) and remains unexplained.

solubility changes accompanying the structural configuration changes. This interesting possibility requires specific experimental studies but we consider that at this stage, experimental and theoretical constraints are too weak to allow our model to ascribe different effects to differences in the valence state of iron.

3.6. The effect of melt structure on CO_2 solubility

In this last part, we clarify the crucial role of melt structure and chemistry on CO_2 solubility. Fig. 9 discriminates the effect on CO_2 solubility, as predicted by our model, of NBO species that are bonded to different types of cations:

the calculated solubility of CO_2 at 2000 bar is shown for a MOR-basalt, to which different modifier cations (Na + K, Ca, Mg + Fe) are added in variable amounts. Adding modifier cations results in an increase in NBO/O (with NBO cal-
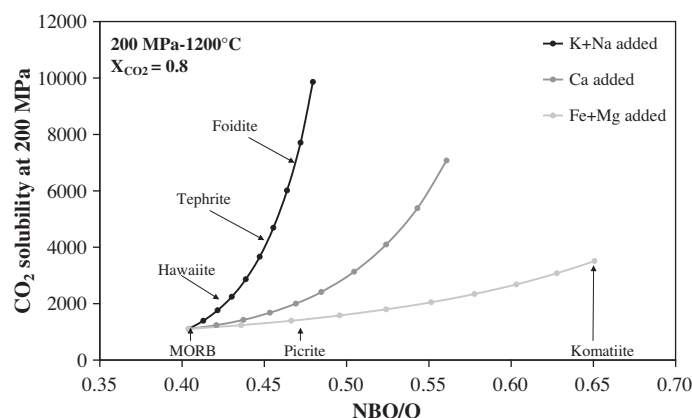

Fig. 9. Calculated effect of NBO/O (with NBO computed on a hydrous basis) on CO_2 solubility at 2000 bar and 1200 °C in equilibrium with a fluid phase containing 80% CO_2. The initial composition (with the lowest NBO/O) is a MORB, with 2 wt% H_2O and a calculated CO_2 solubility of 1100 ppm. The effect of increasing NBO/O is computed considering the addition of different types of modifier cations, which we interpret as the type of cations bonded to the NBO. Cations added are Mg + Fe, Ca, and Na + K. Mg + Fe are added with incremental steps of 2 wt% FeO + MgO (marked by the points on the grey curve), Ca is incremented with step of 1.5 wt% and Na + K are incremented with steps of 1 wt% (0.5 wt% Na_2O, 0.5 wt% K_2O).
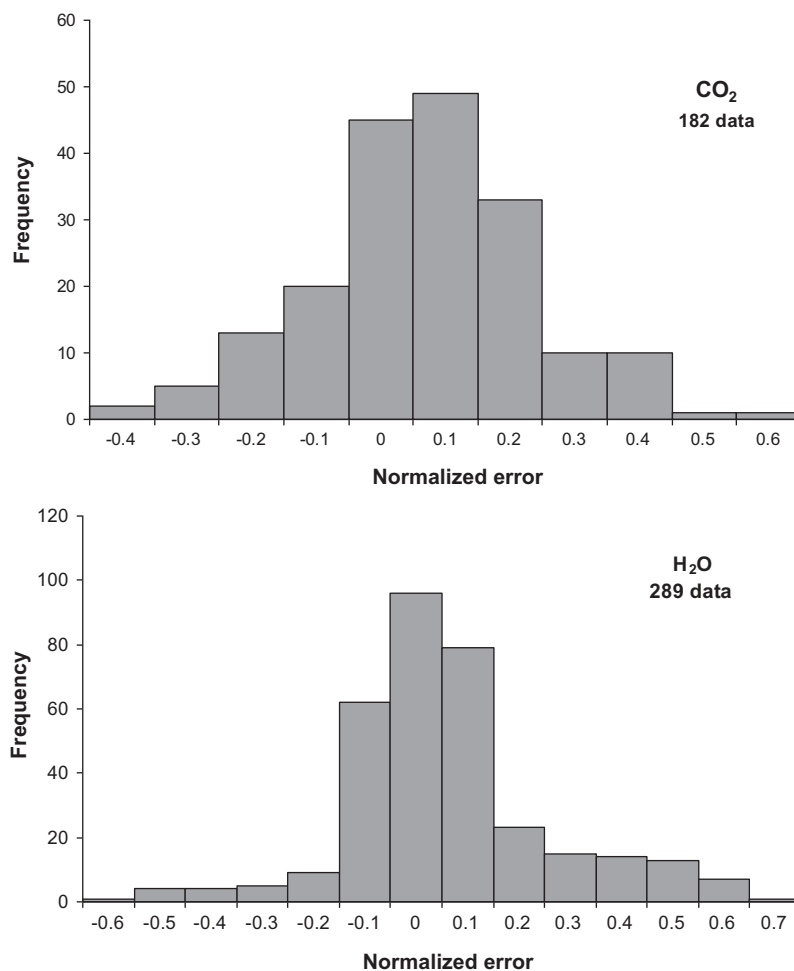

Fig. A1. Frequency distribution of the normalised error (difference between experimental and calculated value, normalised to calculated) for both CO_2 and H_2O models.

culated on a hydrous basis) and therefore in an increase in CO_2 solubility, but the intensity of the effect depends on the type of cation that is added (Fig. 9). Addition of Mg + Fe has less effect on CO_2 solubility. Despite the negative $d_{MgO+FeO}$ in Eq. (6) (Table 5), addition of these cations to basalt slightly increases CO_2 solubility, because their impact on NBO/O dominates over their negative coefficient ($d_{MgO+FeO}$). At the Mg + Fe enrichment level comparable to that of Komatiite compositions or primitive Martian basalts, CO_2 solubility is calculated to be three times higher than that of a MORB. Calcium addition increases more CO_2 solubility than Mg + Fe. Its effect in our Eq. (12) is accounted for by the NBO/O terms and the agpaitic index, $Al_2O_3/(CaO + Na_2O + K_2O)$. Alkalis have the strongest effect on CO_2 solubility: an increase in the alkali content similar to that occurring from a MORB to a foidite enhances CO_2 solubility by a factor of 7.

In a recent paper, Guillot and Sator (2011) investigated the structure and energetic properties of CO_2 incorporation in basalts at high pressure using molecular dynamics simulations. Their theoretical approach is broadly consistent

with our conclusion based on empirical fitting in a melt structure framework. We nevertheless note that the order of preferential cation-NBO-CO_3^{2-} association slightly differs from ours, but Guillot and Sator (2011) did not systematically investigate the effect of variable chemical composition as we did here and their conclusions are based on simulations performed at high pressure ($\gg$1.0 GPa), which makes thorough comparisons difficult.

4. CONCLUSIONS

In this paper, we report new H_2O–CO_2 solubility in mafic melts data that essentially highlight the role of melt composition and structure on CO_2 solubility. These new experimental points show that K-rich and Ca-rich melts have high CO_2 solubility that existing models cannot quantitatively reproduce. In contrast, water solubility is reasonably well accounted for by existing models, whatever the melt composition. We propose a semi empirical model accounting for changes in melt chemical composition on
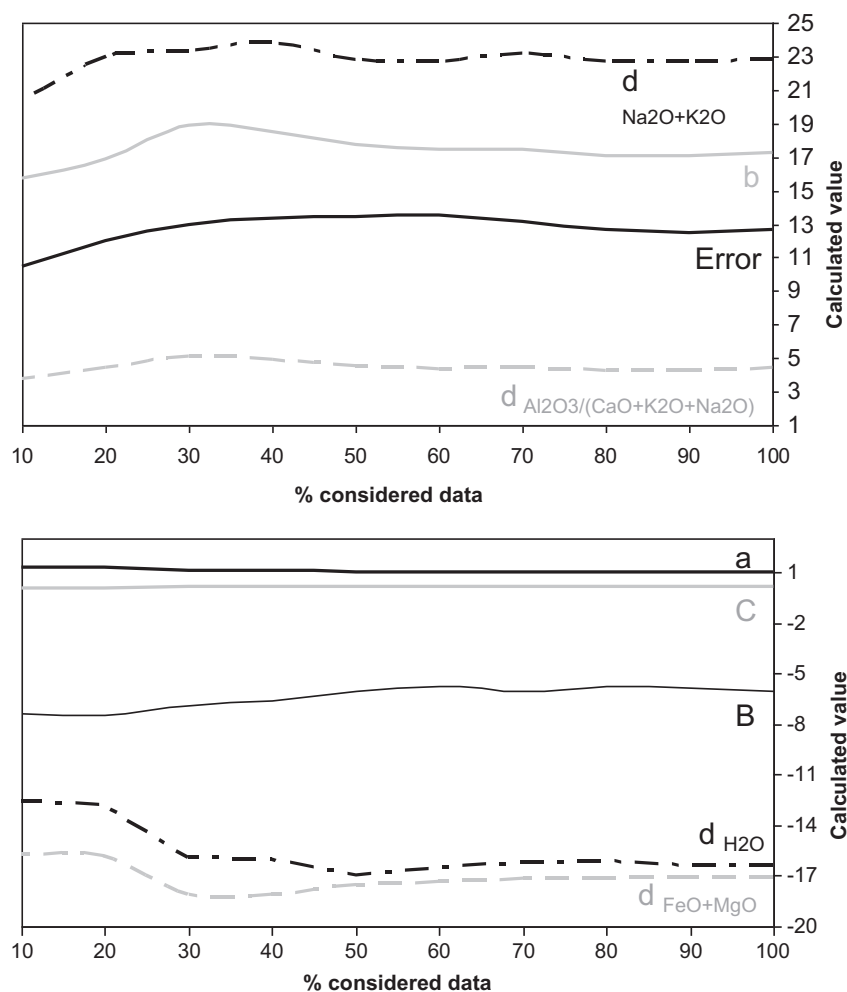

Fig. A2. Variation of the calibrated parameters for CO_2 as a function of the portion of the database considered for the model calibration (selected randomly).

CO_2 solubility by employing melt structural units. Solubility of CO_2 is strongly enhanced by increasing NBO species and this effect increases in efficiency when $Fe + Mg - NBO$, $Ca–NBO$, alkali–NBO pairs occur (in this respective order). Water also appears to enhance CO_2 solubility, especially at high water contents.

A web application of the presented model is available at the following address: https://www.calcul.isto.cnrs-orleans.fr/apps/h2o-co2-systems/.

APPENDIX A

A.1. Calculation of NBO

On an anhydrous basis (following Marrocchi and Toplis, 2005):

$$NBO = 2 \times (X_{K2O} + X_{Na2O} + X_{CaO} + X_{MgO} + X_{FeO} - X_{Al2O3})$$

$$NBO/O = NBO/(2 \times X_{SiO2} + 2 \times X_{TiO2} + 3 \times X_{Al2O3} + X_{MgO} + X_{FeO} + X_{CaO} + X_{Na2O} + X_{K2O})$$

On a hydrous basis:

$$NBO = 2 \times (X_{H2O} + X_{K2O} + X_{Na2O} + X_{CaO} + X_{MgO} + X_{FeO} - X_{Al2O3})$$

$$NBO/O = NBO/(2 \times X_{SiO2} + 2 \times X_{TiO2} + 3 \times X_{Al2O3} + X_{MgO} + X_{FeO} + X_{CaO} + X_{Na2O} + X_{K2O} + X_{H2O})$$

where X is the mol fraction of the different oxides. We considered that all iron is in ferrous form in absence of robust information from the literature database on oxygen fugacity and ferric-ferrous ratios for gas–melt equilibria of Table 4.

A.2. Model error

The model error (13% for CO_2 and% 17% for H_2O) is the average of the error of each data point calculated as:

$100 * |$measured solubility

$- $ calculated solubility$|/$measured solubility

Fig. A1 shows the frequency distribution of the normalised error (difference between experimental and calculated value, normalised to calculated) for both CO_2 and H_2O models.

Fig. A2 shows how the values of the calibrated parameters for CO_2 vary if a portion of the database is considered for the model calibration, instead of the entire one (i.e. 182 experiments). The model is still stable (i.e. the variations in the calibrated parameters and in the total error are <15%) for half of the data (selected randomly).

REFERENCES

Aiuppa A., Federico C., Giudice G., Gurrieri S., Liuzzo M., Shinohara H., Favara R. and Valenza M. (2006) Rates of carbon dioxide plume degassing from Mount Etna volcano. *J. Geophys. Res.* **111**, B09207.

Behrens H., Misiti V., Freda C., Vetere F., Botcharnikov R. E. and Scarlato P. (2009) Solubility of H_2O and CO_2 in ultrapotassic melts at 1200 and 1250 °C and pressure from 50 to 500 MPa. *Am. Mineral.* **94**, 105–120.

Behrens H. and Gaillard F. (2006) Geochemical aspects of melts: volatiles and redox behavior. *Elements* **2**, 275–280.

Behrens H. (2010) Noble gas diffusion in silicate glasses and melts. *Rev. Mineral. Geochem.* **72**.

Berndt J., Liebske C., Holtz F., Freise M., Nowak M., Ziegenbein D., Hurkuk W. and Koepke J. (2002) A combined rapid-quench and H2-membrane setup for internally heated pressure vessels: description and application for water solubility in basaltic melts. *Am. Mineral.* **87**, 1717–1720.

Blank J. G. and Brooker R. A. (1994) Experimental studies of carbon-dioxide in silicate melts-solubility, speciation, and stable carbon-isotope behavior. *Rev. Mineral.* **30**, 157–186.

Botcharnikov R. E., Freise M., Holtz F. and Behrens H. (2005) Solubility of C–O–H mixtures in natural melts: new experimental data and application range of recent models. *Ann Geophys* **48**, 633–646.

Botcharnikov R. E., Behrens H. and Holtz F. (2006) Solubility and speciation of C–O–H fluids in andesitic melt at T = 1100–1300 °C and P = 200 and 500 MPa. *Chem. Geol.* **229**, 125–143.

Brooker R. A., Kohn S. C., Holloway J. R., McMillan P. F. and Carroll M. R. (1999) Solubility, speciation and dissolution mechanisms for CO_2 in melts on the $NaAlO_2$–SiO_2 join. *Geochim. Cosmochim. Acta* **63**, 3549–3565.

Brooker R. A., Kohn S. C., Holloway J. R. and McMillan P. F. (2001a) Structural controls on the solubility of CO_2 in silicate melts Part I: bulk solubility data. *Chem. Geol.* **174**, 225–239.

Brooker R. A., Kohn S. C., Holloway J. R. and McMillan P. F. (2001b) Structural controls on the solubility of CO_2 in silicate melts Part II: IR characteristics of carbonate groups in silicate glasses. *Chem. Geol.* **174**, 241–254.

Burgisser A., Scaillet B. and Harshvardhan (2008) Chemical patterns of erupting silicic magmas and their influence on the amount of degassing during ascent. *J. Geophys. Res.* **113**, B12204.

Burnham C. W. and Davis N. F. (1971) Role of H_2O in silicate melts.1. P–V–T relations in system $NaAlSi_3O_8$–H_2O to 10 kilobars and 1000 °C. *Am. J. Sci.* **270**, 54–98.

Di Matteo V., Mangiacapra A., Dingwell D. B. and Orsi G. (2006) Water solubility and speciation in shoshonitic and latitic melt composition from Campi Flegrei Caldera (Italy). *Chem. Geol.* **229**, 113–124.

Dixon J. E. (1997) Degassing of alkalic basalts. *Am. Mineral.* **82**, 368–378.

Dixon J. E. and Pan V. (1995) Determination of the molar absorptivity of dissolved carbonate in basanitic glass. *Am. Mineral.* **80**, 1339–1342.

Dixon J. E., Stolper E. M. and Holloway J. R. (1995) An experimental study of water and carbon dioxide solubilities in

mid ocean ridge basaltic liquids. 1. Calibration and solubility models. *J. Petrol.* **36**, 1607–1631.

Edmonds M. and Gerlach T. M. (2007) Vapor segregation and loss in basaltic melts. *Geology* **35**, 751–754.

Farnan I. and Stebbins J. F. (1994) The nature of the glass transition in a silica-rich oxide melt. *Science* **265**, 1206–1209.

Fine G. and Stolper E. (1986) Dissolved carbon-dioxide in basaltic glasses-concentrations and speciation. *Earth Planet. Sci. Lett.* **76**, 263–278.

Fiske P. S. and Stebbins J. F. (1994) The structural role of Mg in silicate liquids: a high-temperature ^{25}Mg, ^{23}Na, and ^{29}Si NMR study. *Am. Mineral.* **79**, 848–861.

Frantz J. D. and Mysen B. O. (1995) Raman spectra and structure of BaO–SiO$_2$, SrO–SiO$_2$ and CaO–SiO$_2$ melts to 1600 °C. *Chem. Geol.* **121**, 155–176.

Gaillard F. and Scaillet B. (2009) The sulfur content of volcanic gases on Mars. *Earth Planet. Sci. Lett.* **279**, 34–43.

Gaillard F., Pichavant M. and Scaillet B. (2003) Experimental determination of activities of FeO and Fe$_2$O$_3$ components in hydrous silicic melts under oxidizing conditions. *Geochim. Cosmochim. Acta* **67**, 4389–4409.

Georges A. M. and Stebbins J. F. (1998) Structure and dynamics of magnesium in silicate melts: A high-temperature ^{25}Mg NMR study. *Am. Mineral.* **83**, 1022–1029.

Ghiorso M. S. and Sack R. O. (1995) Chemical mass-transfer in magmatic processes. 4. A revised and internally consistent thermodynamic model for the interpolation and extrapolation of liquid–solid equilibria in magmatic systems at elevated-temperatures and pressures. *Contrib. Mineral. Petrol.* **119**, 197–212.

Grimmer A. R., Magi M., Hahnert M., Stade H., Samoson A., Wieker W. and Lippmaa E. (1984) High resolution solid state ^{29}Si NMR spectroscopic studies of binary alkali silicate glasses. *Phys. Chem. Glasses* **25**, 105–109.

Guignard M. and Cormier L. (2008) Environments of Mg and Al in MgO–Al$_2$O$_3$–SiO$_2$ glasses: a study coupling neutron and X-ray diffraction and reverse Monte Carlo modelling. *Chem. Geol.* **256**, 111–118.

Guillot B. and Sator N. (2007) A computer simulation study of natural silicate melts. Part I: low pressure properties. *Geochim. Cosmochim. Acta* **71**, 1249.

Guillot B. and Sator N. (2011) Carbon dioxide in silicate melts: a molecular dynamics simulation study. *Geochim. Cosmochim. Acta* **75**, 1829–1857.

Halter W. E. and Mysen B. O. (2004) Melt speciation in the system Na$_2$O–SiO$_2$. *Chem. Geol.* **213**, 115–123.

Hamilton D. L., Burnham C. W. and Osborn E. F. (1964) The solubility of water and effects of oxygen fugacity and water content on crystallization in mafic magmas. *J. Petrol.* **5**, 21–39.

Iacono-Marziano G., Gaillard F. and Pichavant M. (2008) Limestone assimilation by basaltic magmas: an experimental re-assessment and application to Italian volcanoes. *Contrib. Mineral. Petrol.* **155**, 719–738.

Iacono-Marziano G., Gaillard F., Scaillet B., Pichavant M. and Chiodini G. (2009) Role of non-mantle CO2 in the dynamics of volcano degassing: the Mount Vesuvius example. *Geology* **37**, 319–322.

Ihinger P. D., Hervig R. L. and McMillan P. F. (1994) Analytical methods for volatiles in glasses. *Rev. Mineral.* **30**, 67–121.

Jakobsson S. (1997) Solubility of water and carbon dioxide in an icelandite at 1400 °C and 10 kilobars. *Contrib. Mineral. Petrol.* **127**, 129–135.

Jendrzejewski N., Trull T. W., Pineau F. and Javoy M. (1997) Carbon solubility in Mid-Ocean Ridge basaltic melt at low pressures (250–1950 bar). *Chem. Geol.* **138**, 81–92.

Kelsey K. E., Allwardt J. R. and Stebbins J. F. (2008) Ca–Mg mixing in aluminosilicate glasses: an investigation using ^{17}O

MAS and 3QMAS and ^{27}Al MAS NMR. *J. Non-Cryst. Solids* **354**, 4644–4653.

Kerrick D. H. and Jacobs G. K. (1981) A modified Redlick-Kwong equation for H$_2$O, CO$_2$, and H$_2$O–CO$_2$ mixtures at elevated pressures and temperatures. *Am. J. Sci.* **281**, 735–767.

King P. L. and Holloway J. R. (2002) CO$_2$ solubility and speciation in intermediate (andesitic) melts: the role of H$_2$O and composition. *Geochim. Cosmochim. Acta* **66**, 1627–1640.

Kohn S. C., Brooker R. A. and Dupree R. (1991) ^{13}C MAS NMR: A method for studying CO$_2$ speciation in glasses. *Geochim. Cosmochim. Acta* **55**, 3879–3884.

Kroeker S. and Stebbins J. F. (2000) Magnesium coordination environments in glasses and minerals: New insight from high-field magnesium-25 MAS NMR. *Am. Mineral.* **85**, 1459–1464.

Lee S. K. and Sung S. (2008) The effect of network-modifying cations on the structure and disorder in peralkaline Ca–Na aluminosilicate glasses: O-17 3QMAS NMR study. *Chem. Geol.* **256**, 326–333.

Lee S. K. and Stebbins J. F. (2009) Effects of the degree of polymerization on the structure of sodium silicate and aluminosilicate glasses and melts: an ^{17}O NMR study. *Geochim. Cosmochim. Acta* **73**, 1109–1119.

Lesne P. (2008) Etude expérimentale de la solubilité des volatils C–H–O–S dans les basaltes alcalins italiens. Simulations numériques du dégazage chimique: application à l'Etna. Ph. D. thesis.

Lesne P., Scaillet B., Pichavant M., Iacono-Marziano G. and Beny J. M. (2011a) The H2O solubility of alkali basaltic melts: an experimental study. *Contrib. Mineral. Petrol.* **162**, 133–151. http://dx.doi.org/10.1007/s00410-010-0588-x.

Lesne P., Scaillet B., Pichavant M. and Beny J. M. (2011b) The carbon dioxide solubility in alkali basalts: an experimental study. *Contrib. Mineral. Petrol.* **162**, 153–168. http://dx.doi.org/10.1007/s00410-010-0585-0.

Liotta M., Paonita A., Caracausi A., Martelli M., Rizzo A. and Favara R. (2010) Hydrothermal processes governing the geochemistry of the crater fumaroles at Mount Etna volcano (Italy). *Chem. Geol.* **278**, 92–104.

Maekawa H., Maekawa T., Kawamura K. and Yokokawa T. (1991) The structural groups of alkali silicate glasses determined from ^{29}Si MAS NMR. *J. Non-Cryst. Solids* **127**, 53–64.

Maekawa H., Nakao T., Shimokawa S. and Yokokawa T. (1997) Coordination of sodium ions in NaAlO$_2$–SiO$_2$ melts: a high temperature ^{23}Na NMR study. *Phys. Chem. Miner.* **24**, 53–65.

Malfait W. J., Halter W. E., Morizet Y., Meier B. H. and Verel R. (2007) Structural control on bulk melt properties: single and double quantum ^{29}Si NMR spectroscopy on alkali-silicate glasses. *Geochim. Cosmochim. Acta* **71**, 6002–6018.

Marrocchi Y. and Toplis M. J. (2005) Experimental determination of argon solubility in silicate melts: an assessment of the effects of liquid composition and temperature. *Geochim. Cosmochim. Acta* **69**, 5765–5776.

McMillan P. F. and Wilding M. C. (2009) High pressure effects on liquid viscosity and glass transition behaviour, polyamorphic phase transitions and structural properties of glasses and liquids. *J. Non-Cryst. Solids* **355**, 722–732.

Menand T. and Phillips J. C. (2007) Gas segregation in dykes and sills. *J. Volcanol. Geotherm. Res.* **159**, 393–408.

Métrich N. and Rutherford M. J. (1998) Low pressure crystallization paths of H$_2$O-saturated basaltic-hawaiitic melts from Mt. Etna: implications for open-system degassing of basaltic volcanoes. *Geochim. Cosmochim. Acta* **62**, 1195–1205.

Métrich N. and Wallace P. J. (2008) Volatile abundances in basaltic magmas and their degassing paths tracked by melt inclusions. *Rev. Mineral. Geochem.* **69**, 363–402.

Moore G. (2008) Interpreting H_2O and CO_2 contents in melt inclusions: constraints from solubility experiments and modeling. *Rev. Mineral. Geochem.* **69**, 333–361.

Moore G., Vennemann T. and Carmichael I. S. E. (1995) Solubility of water in magmas to 2 kbar. *Geology* **23**, 1099–1102.

Moore G., Vennemann T. and Carmichael I. S. E. (1998) An empirical model for the solubility of H_2O in magmas to 3 kilobars. *Am. Mineral.* **83**, 36–42.

Moretti R. and Papale P. (2004) On the oxidation state and volatile behavior in multicomponent gas–melt equilibria. *Chem. Geol.* **213**, 265–280.

Morizet Y., Paris M., Gaillard F. and Scaillet B. (2010) C–O–H fluid solubility in haplobasalt under reducing conditions: an experimental study. *Chem. Geol.* **279**, 1–16.

Morizet Y., Brooker R. A. and Kohn S. C. (2002) CO_2 in haplophonolite melt: solubility, speciation and carbonate complexation. *Geochim. Cosmochim. Acta* **66**, 1809–1820.

Mysen B. O. and Toplis M. J. (2007) Structural behavior of Al^{3+} in peralkaline, metaluminous, and peraluminous silicate melts and glasses at ambient pressure. *Am. Mineral.* **92**, 933–946.

Mysen B. O., Arculus R. J. and Eggler D. H. (1975) Solubility of carbon dioxide in melts of andesite, tholeiite, and olivine nephelinite composition to 30 kbar pressure. *Contrib. Mineral. Petrol.* **53**, 227–239.

Mysen B. O. (2003) Physics and chemistry of silicate glasses and melts. *Eur. J. Mineral.* **15**, 781–802.

Neuville D. R., Cormier L. and Massiot D. (2006) Al coordination and speciation in calcium aluminosilicate glasses: effects of composition determined by ^{27}Al MQ-MAS NMR and Raman spectroscopy. *Chem. Geol.* **229**, 173–185.

Neuville D. R., Henderson G. S., Cormier L. and Massiot D. (2010) The structure of crystals, glasses, and melts along the $CaO–Al_2O_3$ join: results from Raman, Al L- and K-edge X-ray absorption, and Al-27 NMR spectroscopy. *Am. Mineral.* **95**, 1580–1589.

Newman S. and Lowenstern J. B. (2002) VOLATILECALC: a silicate melt-H_2O–CO_2 solution model written in Visual Basic for excel, Source. *Comput. Geosci.* **28**, 597–604.

O'Neill H. S. C. and Mavrogenes J. A. (2002) The sulphide capacity and the sulphur content at sulphide saturation of silicate melts at 1400 °C and 1 bar. *J. Petrol.* **43**, 1049–1087.

Pan V., Holloway J. R. and Hervig R. L. (1991) The pressure and temperature-dependence of carbon dioxide solubility in tholeiitic basalt melts. *Geochim. Cosmochim. Acta* **55**, 1587–1595.

Papale P. (1997) Modeling of the solubility of a one-component H_2O or CO_2 fluid in silicate liquids. *Contrib. Mineral. Petrol.* **126**, 237–251.

Papale P. (1999) Modeling of the solubility of a two-component $H_2O + CO_2$ fluid in silicate liquid. *Am. Mineral.* **84**, 477–492.

Papale P., Moretti R. and Barbato D. (2006) The compositional dependence of the saturation surface of $H_2O + CO_2$ fluids in silicate melts. *Chem. Geol.* **229**, 78–95.

Pawley A. R., Holloway J. R. and McMillan P. F. (1992) The effect of oxygen fugacity on the solubility of carbon–oxygen fluids in basaltic melts. *Earth Planet. Sci. Lett.* **110**, 213–225.

Peccerillo A., Poli G. and Serri G. (1998) Petrogenesis of orenditic and kamafugitic rocks from Central Italy. *Can. Mineral.* **26**, 45–65.

Phillips J. C. and Woods A. W. (2002) Suppression of large-scale magma mixing by melt-volatile separation. *Earth Planet. Sci. Lett.* **204**, 47–60.

Rossano S., Ramos A. Y. and Delaye J. M. (1999) Environment of ferrous iron in $CaFeSi_2O_6$ glass; contributions of EXAFS and molecular dynamics. *J. Non-Cryst. Solids* **273**, 48–52.

Scaillet B. and Pichavant M. (2003). *Experimental constraints on volatile abundances in arc magmas and their implications for degassing processes.* (pp. 197–182) (Special Publication).

Schneider J., Mastelaro V. R., Zanotto E. D., Shakhmatkin B. A., Vedishcheva N. M., Wright A. C. and Panepucci H. (2003) Qn distribution in stoichiometric silicate glasses: thermodynamic calculations and ^{29}Si high resolution NMR measurements. *J. Non-Cryst. Solids* **325**, 164–178.

Shimoda K., Nemoto T. and Salto K. (2008) Local structure of Magnesium in silicate glasses: a ^{25}Mg 3QMAS NMR study. *J. Phys. Chem. B* **112**, 6747–6752.

Shinohara H., Aiuppa A., Giudice G., Gurrieri S. and Liuzzo M. (2008) Variation of H_2O/CO_2 and CO_2/SO_2 ratios of volcanic gases discharged by continuous degassing of Mount Etna volcano. *Italy. J. Geophys. Res.* **113**, B09203.

Shishkina T. A., Botcharnikov R. E., Holtz F., Almeev R. R. and Portnyagin M. V. (2010) Solubility of H2O- and CO2-bearing fluids in tholeiitic basalts at pressures up to 500 MPa. *Chem. Geol.* **277**, 115–125.

Spera F. J. and Bergman S. C. (1980) Carbon-dioxide in igneous petrogenesis.1. Aspects of the dissolution of CO_2 in silicate liquids. *Contrib. Mineral. Petrol.* **74**, 55–66.

Spilliaert N., Allard P., Metrich N. and Sobolev A. V. (2006) Melt inclusion record of the conditions of ascent, degassing, and extrusion of volatile-rich alkali basalt during the powerful 2002 flank eruption of Mount Etna (Italy). *J. Geophys. Res.* **111**. http://dx.doi.org/10.1029/2005JB003934.

Stolper E. (1982) The speciation of water in silicate melts. *Geochim. Cosmochim. Acta* **46**, 2609–2620.

Stolper E. and Holloway J. R. (1988) Experimental determination of the solubility of carbon-dioxide in molten basalt at low-pressure. *Earth Planet. Sci. Lett.* **87**, 397–408.

Toplis M. J., Dingwell D. B. and Lenci T. (1997) Peraluminous viscosity maxima in $Na_2O–Al_2O_3–SiO_2$ liquids: The role of triclusters in tectosilicate melts. *Geochim. Cosmochim. Acta* **61**, 2605–2612.

Toplis M. J., Kohn S. C., Smith M. E. and Poplett I. J. F. (2000) Fivefold-coordinated aluminum in tectosilicate glasses observed by triple quantum MAS NMR. *Am. Mineral.* **85**, 1556–1560.

Thibault Y. and Holloway J. R. (1994) Solubility of CO_2 in a Ca-rich leucitite- effects of pressure, temperature, and oxygen fugacity. *Contrib. Mineral. Petrol.* **116**, 216–224.

Vetere F., Botcharnikov R. E., Holtz F., Behrens H. and De Rosa R. (2011) Solubility of H_2O and CO_2 in shoshonitic melts at 1250 °C and pressure from 50 to 400 MPa: implications for Campi Flegrei magmatic systems. *J. Volcanol. Geotherm. Res.* **202**, 251–261.

Wallace, P.J. (2003) From mantle to atmosphere: Magma degassing, explosive eruptions, and volcanic volatile budgets. Melt inclusions in volcanic systems: methods, applications and problems. In *Developments in Volcanology*, vol. 5, Publisher: Elsevier Science BV, pp.105–127.

Wallace P. and Carmichael I. S. E. (1992) Sulfur in basaltic magmas. *Geochim. Cosmochim. Acta* **56**, 1863–1874.

Xue X. and Kanzaki M. (2004) Dissolution mechanisms of water in depolymerized silicate melts: constraints from ^{1}H and ^{29}Si NMR spectroscopy and ab initio calculations. *Geochim. Cosmochim. Acta* **68**, 5027–5057.

Zotov N. and Keppler H. (1998) The influence of water on the structure of hydrous sodium tetrasilicate glasses. *Am. Mineral.* **83**, 823–834.

Associate editor: Michael Toplis